Materials Advances

ROYAL SOCIETY OF CHEMISTRY

PAPER

View Article Online
View Journal | View Issue

Cite this: *Mater. Adv.*, 2026, 7, 826

A decoupling strategy to optimize power density in flexible thermoelectric devices using a ZIF-67 doped polypyrrole bio binder-based hybrid ink

Kishor D. Kalarakoppa,[a] A. N. Prabhu, *[a] Ramakrishna Nayak,[b] Nishitha Prabhu,[a] Mohammad Saquib,[c] Shilpa Shetty[c] and Kavya Naik[c]

Received 28th July 2025,
Accepted 17th November 2025

DOI: 10.1039/d5ma00819k

rsc.li/materials-advances

Enhancing the power density of flexible thermoelectric generators for wearable applications is always a challenge. Inclusion of porous material in the active material is one of the attractive strategies deployed to this end. Porosity of a material tunes the thermal conductivity and charge carrier mobility, resulting in enhanced power density. Zeolitic imidazolate framework-67 (ZIF-67) is widely studied for developing gas storage, separation, electrochemical energy storage, sensors, drug delivery systems, membranes, thermal insulations, and triboelectric nanogenerators due to its high thermal and chemical stability, large surface area, and tunable porosity. However, its application for thermoelectric generators has not been explored much. In this work, novel hybrid thermoelectric inks were formulated by integrating zeolitic imidazolate framework-67 (ZIF-67) into a conductive polypyrrole matrix, aiming to fabricate high-performing flexible thermoelectric generators using the screen-printing technique for low-temperature applications. The optimized 5% ZIF-67 ink-based flexible thermoelectric generator, in comparison with the pristine polypyrrole-based device, exhibits 328.6% higher power density. Additionally, a 5% ZIF-67-MnO_2 based p–n type FTEG exhibited a Seebeck coefficient of 171.6 μV K^{-1} and a power output of 26 nW. These results demonstrate the potential of ZIF-67-polypyrrole hybrid inks for eco-friendly, flexible energy harvesting applications.

1. Introduction

Enormous amounts of waste heat are liberated from industrial processes, transportation, and electronic devices, resulting in huge amounts of untapped energy. Thermoelectric generators (TEGs) are solid-state devices that convert this waste heat directly into electricity through the phenomenon of the Seebeck effect.[1] Their compact design, lack of moving parts, silent operation, and low maintenance make them especially attractive for applications ranging from automotive exhaust systems to wearable electronics and renewable energy systems.[2]

From a materials science perspective, conductors, semiconductors, and insulators exhibit distinct behaviours concerning thermoelectric performance. Conductors such as copper and silver possess high electrical conductivity but suffer from low Seebeck coefficients. Semiconductors, on the other hand, offer a more favourable balance. With moderate electrical conductivity and Seebeck coefficients often reaching several hundred μV K^{-1}. Insulators like MOFs[3] are characterized by a large band gap, resulting in negligible electrical conductivity due to the absence of free charge carriers. Consequently, when combined with polymers, they are effective in generating a thermoelectric voltage and are suitable for thermoelectric applications.[4] This technique allows precise control over material distribution and can integrate multiple functionalities into a single device. Even though conventional TEGs are explored widely due to their exceptional conductivity, wide temperature range, and remarkable thermoelectric performance,[5,6] they lag because of their rigid structure, toxicity, and expensive fabrication techniques.

To overcome these limitations, flexible thermoelectric generators (FTEGs) have emerged. Because of their simple design, versatility, and ability to bend, they have paved their way into wearable electronics, self-powered sensors, Internet of Things (IoT) devices,[7] and cardiac pacemakers.[8,9] Although printed TE devices often exhibit lower power output than bulk or 3D materials,[10] they offer advantages such as low-cost mass production, mechanical flexibility, and environmental friendliness. Thermoelectric (TE) performance strongly depends on three key parameters: the Seebeck coefficient, electrical conductivity, and

[a] *Department of Physics, Manipal Institute of Technology, Manipal Academy of Higher Education, Manipal, Karnataka, 576104, India. E-mail: ashwatha.prabhu@manipal.edu*
[b] *Department of Humanities and Management, Manipal Institute of Technology, Manipal Academy of Higher Education, Manipal, Karnataka, 576104, India*
[c] *Department of Chemistry, Manipal Institute of Technology, Manipal Academy of Higher Education, Manipal, Karnataka, 576104, India*

thermal conductivity, which together determine the material's figure of merit (*ZT*). Recent advances in two-dimensional (2D) materials have enabled better control of charge and heat transport at the nanoscale, enhancing TE efficiency.[11] Enhancing thermoelectric performance involves several strategies, including choosing suitable materials, optimizing surface area (porosity), alloying, doping, utilizing composite and hybrid materials, operating temperature optimization, annealing, and using binders. Porosity increases surface area, enabling more effective phonon scattering and reducing thermal conductivity, which directly improves the thermoelectric figure of merit. Recent developments show that incorporating designed porosity, particularly through structures organized at different scales or with tunable pore architectures, can improve both flexibility and thermoelectric efficiency. This shift from rigid bulk materials to flexible thin film architectures is key to advancing the development of lightweight, wearable TEG devices.[12,13]

In this context, metal–organic frameworks (MOFs) offer a promising solution. MOFs are porous, crystal-like materials with large surface areas, adjustable structures, low thermal conductivity, and customizable electrical properties.[14,15] Even though MOFs have been rarely used in FTEGs because of their insulating properties, they show exceptional improvements in their charge carrier transport, electrical conductance, and thermoelectric performance when doped with guest molecules like polymers and carbon materials.[16,17] For example, Ebrahim *et al.* synthesized a composite of Zr-MOF/polyaniline for thermoelectric applications. The composite achieved the highest *ZT* value of 0.015 and a lower thermal conductivity of 0.24 W m^{-1} K^{-1}.[18] Xu *et al.* studied the photosynthetically modified PANI/MOF, which showed a Seebeck coefficient of 66.6 μV K^{-1}. The author also concluded that doping PANI improved the electronic conductivity and stability.[19] Lin *et al.* synthesized an MOF/carbon nanotube-based p–n type thermoelectric hybrid, comparing the effect of the variation of MOFs (MIL-68 and MIL-53) on carbon films. The films showed a lower thermal conductivity of 0.18 W m^{-1} K^{-1} and 1.3 W m^{-1} K^{-1}. The films also achieved the highest figure of merit of 0.071 and 0.025. The 7 paired devices exhibited a maximum power of 165.5 nW.[20]

To address this gap, we propose a new approach by combining zeolitic imidazolate framework-67 (ZIF-67), a cobalt-based MOF, with PPy to create printable hybrid inks for flexible thermometric devices. ZIF-67 was chosen for its high porosity, chemical stability, and ability to enhance conductivity when mixed with polymers. Considering these properties, ZIF-67 is found to have various applications in fields such as IoT devices, sensors, energy storage, and harvesting devices.[21–23] Yuan *et al.* (2021) showed that adding PPy to ZIF-67 greatly improved its electrical conductivity.[16]

This work presents a novel FTEG based on screen-printed inks formulated from PPy doped with varying concentrations of ZIF-67 through a cost-effective screen-printing technique. Screen printing is appealing for flexible device fabrication, offering simplicity, scalability, and compatibility with various substrates, as demonstrated by previous studies on FTEGs.[17,24] Moreover, using environmentally benign solvents and binders such as dimethylformamide (DMF) and cellulose acetate propionate (CAP) aligns the fabrication process with green chemistry principles.[24] Meanwhile, the use of ZIF-67 in energy harvesting systems has also been validated in nanogenerators, where it contributes to enhanced voltage and current output due to its high dielectric constant and triboelectric behavior.[25] The novelty of this work lies in the innovative integration of ZIF-67 with PPy to develop printable hybrid inks for flexible thermoelectric energy harvesting.

1.1 Materials and methods

In this study, pyrrole (99% purity) was procured from Spectrochem, and sodium lauryl sulphate (SLS, $C_{12}H_{25}NaSO_4$, 97% purity), ferric chloride hexahydrate ($FeCl_3{\cdot}6H_2O$, 97% purity), cobalt(II) nitrate hexahydrate ($Co(NO_3)_2{\cdot}6H_2O$, 97% purity), 2-methylimidazole ($C_4H_6N_2$, 98% purity), methanol (99.9% purity), ethanol and diacetone alcohol (DAA, 98% purity) were purchased from LOBA Chemie Pvt. Ltd. Cellulose acetate propionate (CAP, 99% purity) and *N*, *N*-dimethyl formamide (DMF, 99% purity) were purchased from Sigma-Aldrich. All chemicals were used as received, without further purification. A transparent, flexible polyethylene terephthalate (PET) film with a thickness of 0.100 mm was used as the substrate. Screen printing silver ink (Loctite ECI 1010 E&C), was obtained from Henkel, India.

1.2 Synthesis of zeolitic imidazolate framework-67

ZIF-67, as shown in Fig. 1, was synthesized using a chemical synthesis approach reported elsewhere, in which 1.43 g of ($Co(NO_3)_2{\cdot}6H_2O$) was dissolved in 50 mL of methanol, and 3.24 g of $C_4H_6N_2$ was separately dissolved in another 50 mL of methanol.[21] The two solutions were combined and stirred in a magnetic stirrer for 30 minutes to ensure thorough mixing. The resulting mixture was left undisturbed for 24 hours (h) to facilitate the formation of the complex. Subsequently, the methanol and solid products were separated by centrifugation. The obtained purple solid product was then dried at 60 °C for 6 h.

1.3 Synthesis of polypyrrole

PPy was synthesized using a chemical synthesis method, in which a suspension of 0.33 g of pyrrole in 50 mL of deionized (DI) water was prepared. This suspension was stirred in a magnetic stirrer for 10 min at room temperature, and 0.32 g of SLS was dissolved separately in 50 mL of DI water. The two solutions were then mixed and stirred in a magnetic stirrer for 30 minutes at room temperature. Afterwards, a solution of 1.35 g of $FeCl_3{\cdot}6H_2O$ in 50 mL of distilled water was added dropwise to the above mixture. The solution was stirred for 5 h after the addition of $FeCl_3{\cdot}6H_2O$. The solution was then subjected to vacuum filtration, rinsed with DI water and ethanol several times, and dried at 60 °C for 6 h.

1.4 Synthesis of ZIF-67 doped polypyrrole composites

Fig. 2 represents the synthesis route for ZIF-67 doped PPy composites, which were prepared using the chemical synthesis method. A suspension of 0.33 g of pyrrole in 50 mL of DI water was prepared and stirred in a magnetic stirrer for 10 min at room temperature. Later, 0.32 g of SLS was dissolved separately in 50 mL of DI water. Then, the two solutions were mixed and stirred in a magnetic

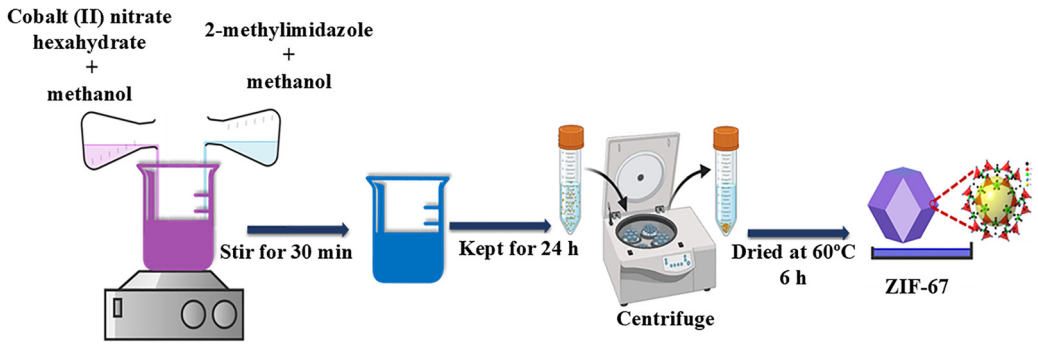

Fig. 1 Schematic illustration of the synthesis of ZIF-67 *via* a solvothermal method.

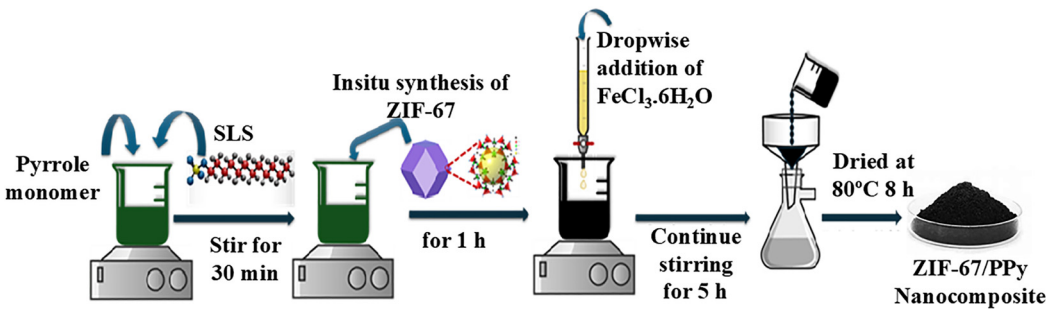

Fig. 2 Synthetic route of the ZIF-67/PPy composites showing *in situ* polymerization of pyrrole on ZIF-67 surfaces to form conductive hybrids.

Table 1 Composition of the PPy:ZIF-67 composites

Composite name	ZIF-67 (wt%)	Polypyrrole (wt%)
PPy	0	100
ZP2.5	2.5	97.5
ZP5	5.0	95.0
ZP10	10.0	90.0

Table 2 ZIF-67/PPy ink compositions

Ink name	ZIF-67/PPy (g)	Ink vehicle (g)
PI	0.11	1.24
ZPI-2.5	0.11	0.99
ZPI-5	0.11	0.99
ZPI-10	0.11	0.99

stirrer for 30 minutes at room temperature. To this mixture, 0.02 g of ZIF-67 (cobalt 2-methylimidazole) was added, and the mixture was stirred for an additional 1 h. The mixture was then placed in an ice bath, and a solution of 1.35 g of $FeCl_3{\cdot}6H_2O$, which was dissolved in 50 mL of DI water, was slowly added as an oxidant. The resulting mixture was stirred for 5 h, leading to the formation of a black precipitate. The composite solution was filtered using vacuum filtration, washed with DI water and ethanol several times, and dried at 80 °C for 8 h. Similarly, other composites of PPy: ZIF-67 were prepared with varying concentrations of PPy and ZIF-67 as presented in Table 1.

1.5 Formulation of inks and fabrication of FTEGs

To formulate the ink, the synthesized materials were finely ground, sieved, and mixed with a suitable binder consisting of 80% DMF and 20% CAP. The composition of the prepared ZIF-67/PPy inks is depicted in Table 2. The stencil for screen printing was prepared by coating a screen mesh with a photosensitive emulsion, which was then exposed to UV light through a patterned mask to create the desired design. To fabricate the FTEGs, the prepared inks were applied to the screen and transferred onto a PET substrate by pressing it through the mesh using a squeegee, forming a uniform and conducting layer as shown in Fig. 3.

1.6 Characterization of the materials and FTEGs

X-ray diffraction (XRD) analysis of the synthesized materials was performed using a Rigaku Mini flex 600 (5th generation) with a scanning rate of 2° min^{-1} and a scanning range of 0°–80°. A ZEISS EVO MA18 system, equipped with an Oxford instruments X-act energy dispersive X-ray spectroscopy (EDS) detector, was used to investigate the surface morphology of the samples and the screen-printed flexible thermoelectric generators (FTEGs). The particle size of ZIF-67 was subsequently analyzed using ImageJ software. The chemical composition of the composite was analyzed using a Thermosphere Nexsa XPS instrument, with an Al Kα source. The UV analysis was carried out using a PerkinElmer UV Winlab spectrometer. FTIR spectra of all the samples were analyzed using the Jasco FTIR

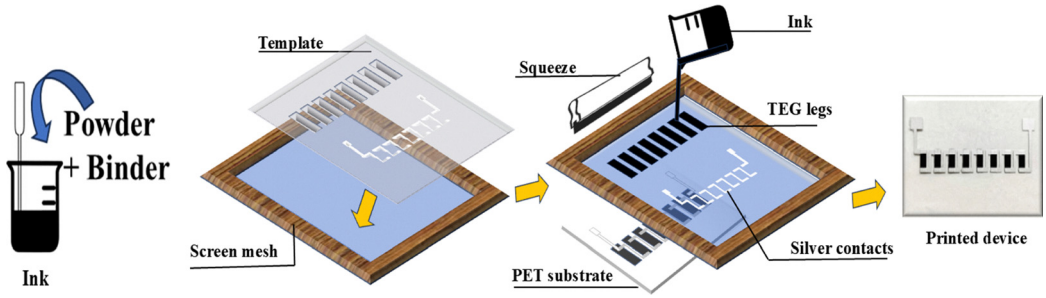

Fig. 3 Formulation process of the ZIF-67/PPy-based ink and fabrication steps for the flexible thermoelectric generator (FTEG) device.

spectrometer. The surface area of the synthesized ZIF-67 and composite materials was determined using a BelsorpminiX. A Brookfield digital viscometer with Spindle S-18 and Ossila goniometer was employed to analyse the rheological properties, such as viscosity and the contact angle of the prepared inks. A square-shaped printed ink film sample of 10 mm×10 mm size was used to study the Hall effect using the Hall effect 3706-A switch. To evaluate the thermoelectric performance of the FTEGs, the hot side was clamped between two copper plates and heated using a digitally controlled hot plate, by varying the temperature of the hot end of the FTEG from room temperature to 135 °C, the cold side was maintained at ambient temperature, as illustrated in Fig. 4. The temperatures on both sides were monitored using a K-type electronic thermocouple (Lutron TM-902C). The thermoelectric voltage generated across the FTEG was measured using a precision Keithley 2001 digital multimeter. The FTEGs were subjected to external load resistances measured using a digital multimeter, and were also tested for their flexibility by measuring the resistance during different bending angles as reported elsewhere.[26]

2. Results and discussion

2.1 X-ray diffraction analysis

X-ray diffraction (XRD) analysis was performed to examine the crystallographic structure, phase purity, and potential structural modifications of the synthesized ZIF-67 and its composites. This characterization is crucial for evaluating the impact of the interaction between ZIF-67 and PPy on crystallinity and structural stability. Diffraction patterns were spanned at a 2θ range of 5° to 40° with a step size of 0.02. Phase identification was carried out using the Crystallography Open Database (COD) number 7247762. The XRD pattern of pristine ZIF-67 shown in Fig. 5(a) exhibited distinct diffraction peaks at 2θ values of 7.3°, 10.4°, 12.7°, 14.7°, 16.5°, and 18.0°, which correspond to the (011), (002), (112), (022), (013) and (222) crystallographic planes, respectively.[27]

These peaks confirm the high crystallinity and phase purity of ZIF-67, consistent with its cubic crystal structure with space group $I\bar{4}3m$. The lattice parameter calculated using Bragg's law was 17.1 Å, closely matching the reported values of $a = b = c \approx 16.9$ Å.[28] Furthermore, the average crystallite size of pristine ZIF-67, PPy and its composites (Table 3) was calculated using the Debye–Scherrer equation,[29] as shown in eqn (1), while the average dislocation densities (δ) and microstrain (ε) were calculated using eqn (2) and (3), respectively.

$$D = \frac{k\lambda}{\beta \cos\theta} \quad (1)$$

$$\delta = \frac{1}{D^2} \quad (2)$$

$$\varepsilon = \frac{\beta}{4 \tan\theta} \quad (3)$$

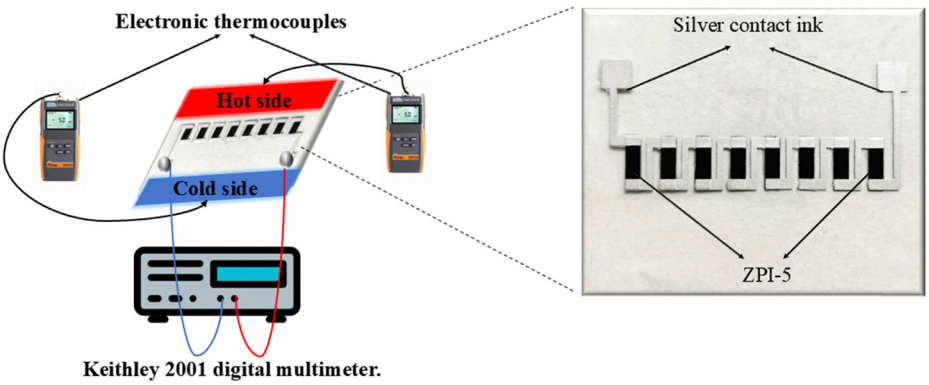

Fig. 4 Experimental setup used for thermoelectric characterization of FTEGs.

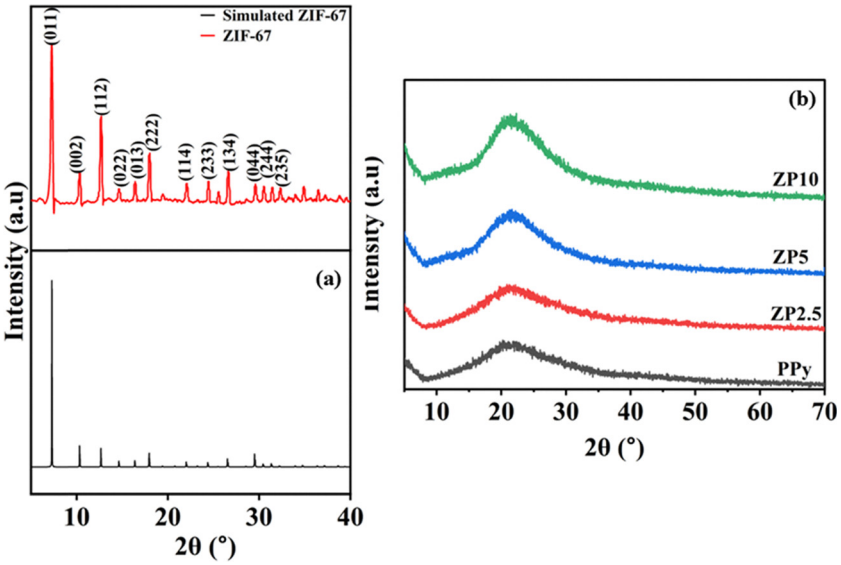

Fig. 5 XRD spectra of (a) ZIF-67, (b) PPy, and (c) ZIF-67/PPy composites.

Table 3 Structural parameters of ZIF-67, PPy, and its composites

Materials	Crystallite size t (nm)	Dislocation density (δ)	Microstrain (ε) 10^{-3}
ZIF-67	50.47	0.41	4.85
PPy	36.03	0.77	4.94
ZP2.5	36.51	0.75	4.86
ZP5	43.13	0.53	4.14
ZP10	46.14	0.46	3.86

where λ – wavelength of X-ray, β – full width half maxima (FWHM), θ – Bragg's diffraction angle, and k – 0.94.

The PPy polymer exhibits a characteristic broad peak centered at $2\theta = 18^{\circ}$–30°, shown in Fig. 5(b). The highest intensity peak at 21.04°, typically attributed to the (020) plane, reflects the amorphousness of the polymer.[30] This broad peak is due to the short-range ordering of π–π stacking interactions between the PPy chains, which shows that pyrrole was polymerized successfully to PPy.[31] The intensity of the broad peak is found to increase with increasing concentration of ZIF-67, revealing the incorporation of ZIF-67 into the polymer matrix.[16]

Table 3 depicts the changes in lattice parameters with increasing ZIF-67 concentration. This variation confirms the successful incorporation of ZIF-67 into the polymer network. However, the inculcation of ZIF-67 has increased the crystallite size, reducing its dislocation density and microstrain, indicating minimal lattice distortion. Also, an enhancement in the crystallite size indicates good crystalline properties, making them exhibit good thermoelectric properties,[32] like electrical conductivity. And the decrease in microstrain may improve the elastic properties in the doped sample.[33]

2.2 Scanning electron microscopy analysis

Fig. 6(a)–(c) shows the surface morphology and microstructural evolution of ZIF-67, PPy, and their composites, respectively. The images reveal distinct morphological characteristics, with pristine ZIF-67 exhibiting a well-defined rhombic dodecahedral shape. The average particle size of ZIF-67 was measured using ImageJ software and was found to be around 417.5 nm with a sigma of 66.89, as shown in Fig. 6(d), indicating high crystallinity. These well-faceted structures confirm the morphology of ZIF-67.[34] In contrast, pure PPy has a homogeneous granular structure composed of interconnected spherical particles, creating a continuous network, indicating its amorphous nature.[35] Upon polymerization with PPy, significant morphological transformations are observed. The previously sharp-edged ZIF-67 particles become coated with a granular polymer layer, leading to a roughened and porous structure.

The magnified images indicate that the polymerization process results in the formation of a continuous and interconnected polymer matrix covering the ZIF-67 particles. This modification suggests strong interfacial interaction between ZIF-67 and the PPy polymer.[36] To complement the SEM analysis, Energy Dispersive X-ray Spectroscopy (EDX) was performed to confirm the elemental composition of the materials. The EDX spectrum identifies characteristic peaks corresponding to cobalt (Co) and nitrogen (N) from ZIF-67, along with carbon (C) and nitrogen (N) originating from the PPy matrix.

The SEM analysis also confirms the successful synthesis of the ZIF-67/PPy composite, which exhibits a significantly roughened and porous morphology. The transformation of smooth dodecahedral ZIF-67 particles to highly textured and polymer-coated composites (Fig. 6(c)) indicates strong interfacial adhesion and structural synergy between the two components.[37]

2.3 Fourier transform infrared spectroscopy analysis

The Fourier transform infrared (FTIR) spectroscopy analysis of ZIF-67, PPy, and their composites was conducted. Fig. 7 provides critical insights into the molecular interactions and structural modifications within these materials. In the ZIF-67

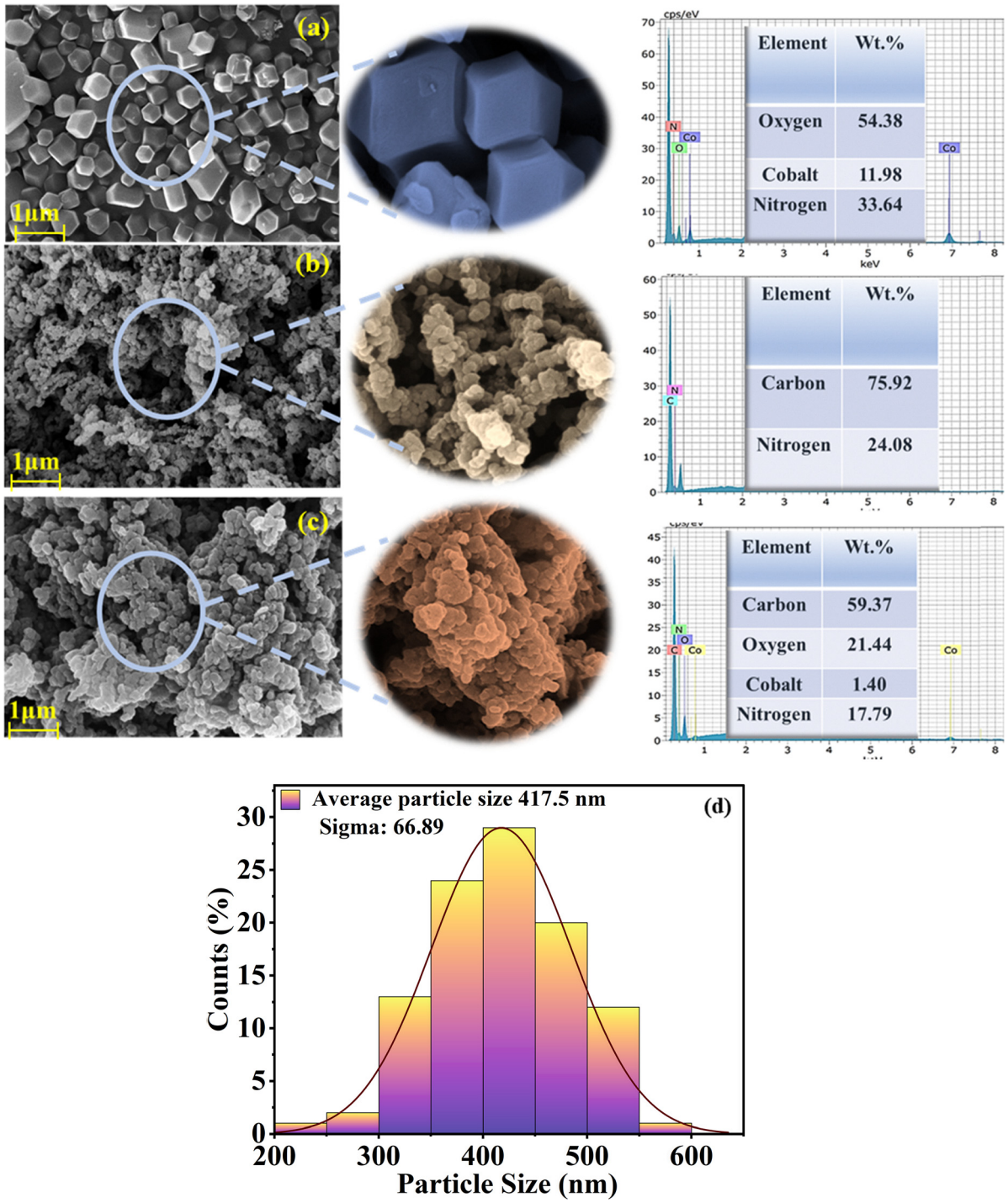

Fig. 6 SEM images of (a) ZIF-67, (b) PPy, and (c) the ZIF-67/PPy composite showing surface morphology, and (d) particle size distribution of ZIF-67.

spectrum, the peak at 2924 cm^{-1} corresponds to the C–H stretching vibration of the methyl imidazole group, while the broad peak at 3441 cm^{-1} indicates O–H stretching. The peaks at 1633 cm^{-1} and 1417 cm^{-1} are attributed to C=N and C=C stretching vibrations of the imidazole ring, respectively. The Co–N vibration appears at 424 cm^{-1}, and the peak at 990 cm^{-1} is associated with plane bending vibrations.[38–40]

On the other hand, the structure of PPy is confirmed by the presence of characteristic FTIR peaks. The peak at 1545 cm^{-1} corresponds to C=C stretching vibrations in the pyrrole ring, while the broad band at 3436 cm^{-1} is attributed to O–H stretching. The peak at 2921 cm^{-1} arises from C–H stretching vibrations. A band at 1309 cm^{-1} indicates C=N stretching, and peaks at 1039 cm^{-1} and 908 cm^{-1} are associated with aromatic

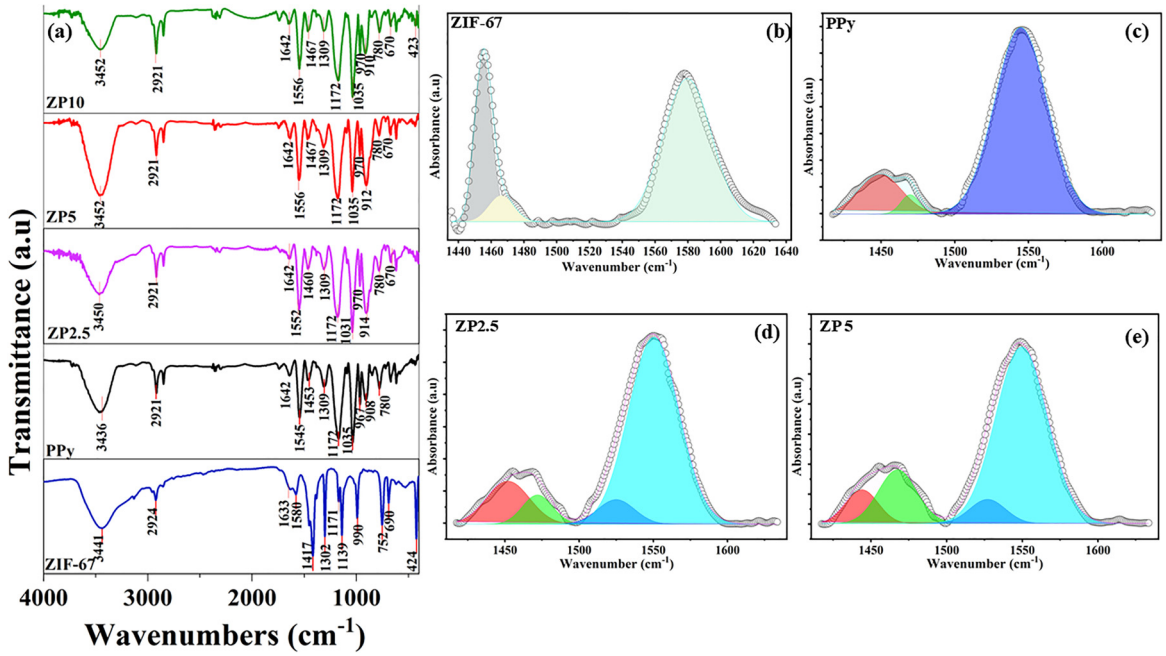

Fig. 7 (a) FTIR spectra of ZIF-67, PPy, and its composites. FTIR deconvolution of (b) ZIF-67, (c) PPy, (d) ZP2.5, and (e) ZP5.

ring bending. Additionally, the peak at 780 cm^{-1} provides evidence of pyrrole polymerization.[41–43]

Upon doping ZIF-67 into the PPy matrix, the FTIR spectra of the ZP2.5, ZP5, and ZP10 composites show notable modifications, indicating successful integration. The broad OH stretching peak around 3441–3436 cm^{-1} remains prominent, while redshifts and intensity variations in C=C at 1545 cm^{-1} and C=N/C=C at 1633 and 1417 cm^{-1} vibrations suggest strong π–π stacking interactions and hydrogen bonding involving ZIF-67. To gain quantitative insights into the molecular interactions between ZIF-67 and PPy, the overlapping C=C and C=N stretching bands in the 1400–1620 cm^{-1} region were deconvoluted using Gaussian fitting, Fig. 7(b)–(e). The pristine ZIF-67 exhibited a strong C=N stretching vibration centered at approximately 1580 cm^{-1}, while PPy showed a dominant C=C stretching peak near 1545 cm^{-1}. Upon forming ZP composites, these characteristic bands progressively redshifted to lower wavenumbers of ~1574 cm^{-1} for C=N and ~1540 cm^{-1} for C=C, accompanied by noticeable changes in peak area and full width at half maximum (FWHM). The systematic redshift and band broadening indicate enhanced π–π electron delocalization and interfacial coupling between the imidazolate ring of ZIF-67 and the conjugated pyrrole backbone. The magnitude of the shift increased with higher PPy content, ZP2.5 to ZP5, confirming stronger electronic interactions and improved charge transfer pathways within the hybrid framework. Enhanced C=N stretching vibrations at 1172 and 1035 cm^{-1}, particularly in ZP5 and ZP10, indicate increased electron delocalization within the composite. Additionally, the appearance of Co–N vibration bands near 424 cm^{-1} confirms the successful incorporation of ZIF-67 into the polymer matrix.[44]

2.4 X-ray photoelectron spectroscopy analysis

Fig. 8(a)–(e) depicts the X-ray photoelectron spectroscopy (XPS) survey spectrum, and Co 2p, N 1s, C 1s, and O 1s spectra, respectively. XPS confirms the chemical composition and valence states of elements in the as-synthesized ZP5. The broad binding energy XPS survey spectrum (Fig. 8(a)) confirms the existence of cobalt, nitrogen, oxygen, and carbon. The well-defined cobalt 2p spectrum is deconvoluted into four peaks corresponding to Co $2p_{3/2}$ and Co $2p_{1/2}$ at 781.9 eV and 796.8 eV, respectively (Fig. 8(b)). Additionally, there are two satellite peaks at 786.9 eV and 803.5 eV due to shake-up excitations associated with strong 3d-2s electron–electron interactions at higher binding energies. The main Co $2p_{3/2}$ peak at 781.9 eV represents Co^{2+} species in a Co–N coordination environment, while the slight shoulder at higher binding energy (~783–784 eV) indicates the presence of Co^{3+}, suggesting a mixed-valence state of cobalt. Such coexistence of Co^{2+} and Co^{3+} species implies partial surface oxidation and enhanced metal–ligand interactions. This oxidation behavior and mixed-valence cobalt configuration are known to improve carrier density and facilitate charge transport, as observed in ZIF-67-derived composites used in energy devices.[45] The high-resolution nitrogen 1s spectrum is distinguished into two major peaks, one at 399.1 eV signifying the cobalt–nitrogen bond and another peak at 400.18 attributed to the nitrogen present in PPy (Fig. 8(c)).[46,47] The carbon 1s spectrum depicts two distinct peaks, the high-intensity peak at 284.8 eV corresponds to the sp^2 hybridised carbon atoms, and the peak at slightly lower intensity around 285 eV relates to the quinone structure of PPy and carbon–oxygen bonding (Fig. 8(d)). The O 1s spectrum in XPS is deconvoluted into three major peaks at 529.4 eV, 531.5 eV, and 532.7 eV, as shown in Fig. 8(e). The first

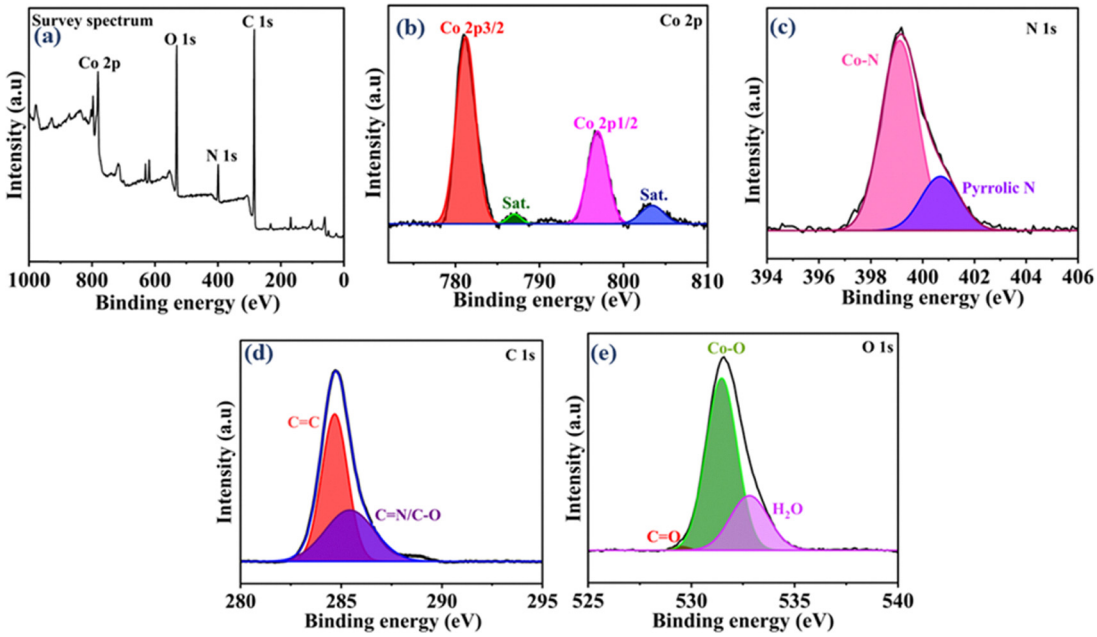

Fig. 8 XPS spectra of ZIF-67 showing (a) survey and high-resolution scans of the (b) Co 2p, (c) N 1s, (d) C 1s, and (e) O 1s regions.

lower intensity peak reveals the presence of the carbonyl oxygen bond, the second high intensity quinone peak defines the cobalt bonding with oxygen (Co–O), and the third peak corresponds to the absorbed oxygen.[48,49]

2.5 Brunauer–Emmett–Teller (BET) analysis

The nitrogen adsorption isotherms of ZIF-67 and ZP5 were analyzed to investigate their surface characteristics and porosity, as shown in Fig. 9(a) and (b). Both samples exhibit Type I isotherms, which are indicative of microporous structures. The BET surface area of ZIF-67 was 1919.5 $m^2\ g^{-1}$, with a total pore volume of 0.6139 $cm^3\ g^{-1}$ and an average pore diameter of 0.6396 nm, confirming its highly porous microporous nature.[50] In contrast, after the incorporation of ZIF-67 into the PPy matrix, a reduction in surface area and porosity was observed. The BET surface area of ZP5 decreased to 39.057 $m^2\ g^{-1}$, with a corresponding pore volume of 0.0211 $cm^3\ g^{-1}$, and the average pore diameter increased from 0.64 to 1.08 nm. The average pore size was determined using the slit-pore model, which correlates the total pore volume and BET surface area. This confirms that the PPy coating blocks a portion of the intrinsic micropores, generating a denser composite with reduced accessible porosity. The change is due to the partial blocking of micropores by the PPy network during composite formation.[18] These results confirm that the PPy incorporation leads to a denser structure, in agreement with the morphological features observed in SEM.

2.6 Hall effect analysis

The Hall effect graphs shown in Fig. 10(a) and (b) present insights into the electronic transport properties of four FTEGs, PI, ZPI-2.5, ZPI-5, and ZPI-10, focusing on carrier concentration, carrier mobility, and electrical conductivity. The p-

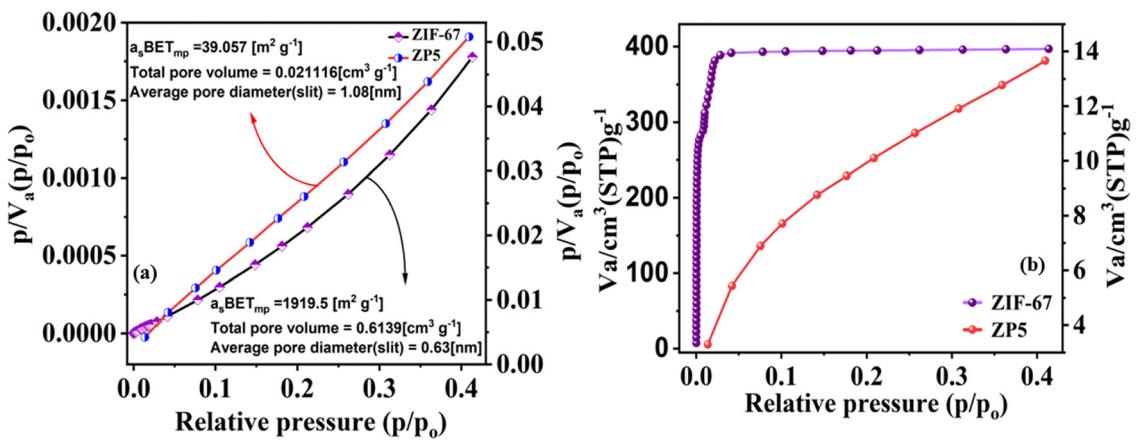

Fig. 9 (a) BET type-I plot and (b) adsorption isotherm of the ZIF-67 and ZP5 composites.

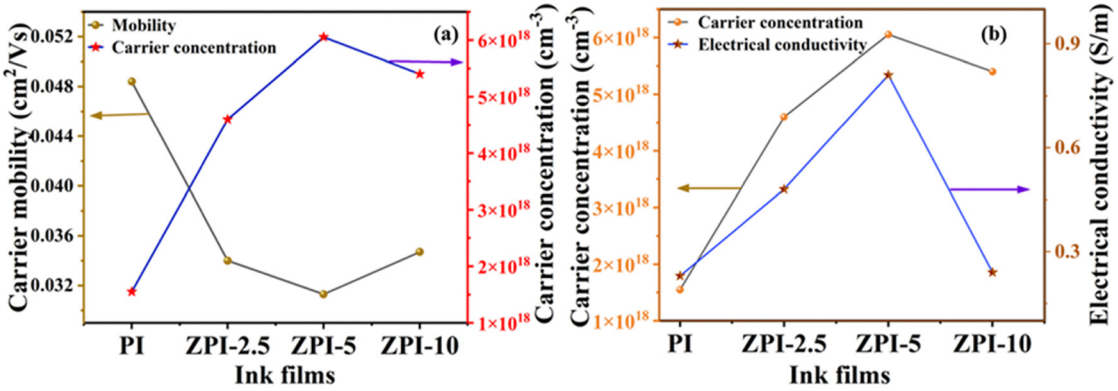

Fig. 10 Comparison of (a) carrier concentration *vs.* electrical conductivity, and (b) carrier mobility *vs.* carrier concentration of PI and ZPI ink film samples.

type behaviour of the materials was confirmed from the positive R_H values of the ink films. Fig. 10(a) provides the relationship between carrier mobility and concentration for all the ink films. In the PI ink film, the highest carrier mobility (0.049 $cm^2\ V^{-1}\ s^{-1}$) is observed, which can be attributed to its relatively ordered structure with fewer scattering sites; however, its low carrier concentration ($1.55 \times 10^{18}\ cm^{-3}$) limits its overall electrical performance. In ZPI-2.5, the carrier concentration increases ($4.6 \times 10^{18}\ cm^{-3}$). Still, mobility decreases (0.034 $cm^2\ V^{-1}\ s^{-1}$), likely due to the introduction of dopants or fillers that disrupt the polymer matrix, causing increased scattering and lowering charge transport efficiency.[51] This trend continues in ZPI-5, which shows the highest carrier concentration ($6.1 \times 10^{18}\ cm^{-3}$) but the lowest mobility (0.031 $cm^2\ V^{-1}\ s^{-1}$). These results support the improvement of the Seebeck coefficient and the power output of the FTEGs.[52] In this work, carrier concentration is found to be directly dependent on crystallite size.

This inverse relationship between carrier concentration and mobility aligns with prior observations,[53] where increased carrier density leads to enhanced carrier–carrier and carrier–defect scattering, ultimately diminishing mobility despite improved conductivity. However, ZPI-10 shows a partial recovery in mobility (0.035 $cm^2\ V^{-1}\ s^{-1}$) and a slight decrease in carrier concentration ($5.3 \times 10^{18}\ cm^{-3}$), indicating that structural modifications in ZPI-10 could have mitigated scattering centers, thereby enhancing carrier mobility slightly, while concurrently leading to a minor reduction in carrier concentration.

Fig. 10(b) shows that the carrier concentration varies linearly with the electrical conductivity. Among the four ink films, ZPI-5 exhibited the highest conductivity (0.81 S m^{-1}) and carrier concentration ($6.1 \times 10^{18}\ cm^{-3}$), reflecting an optimal structure or doping level that maximizes both carrier generation and transport. In the ZPI-5 ink film, the electrical conductivity increased from 0.23 to 0.81 S m^{-1}, and the carrier concentration reached $0.65 \times 10^{18}\ cm^{-3}$ from $1.55 \times 10^{18}\ cm^{-3}$. Beyond this, in the ZPI-10, electrical conductivity and carrier concentration increase up to 0.24 S m^{-1} and $5.4 \times 10^{18}\ cm^{-3}$, respectively. The increase in conductivity and carrier concentration suggests that the modification of PPy by additives or dopants has introduced more charge carriers and enhanced charge transport pathways within the polymer matrix.

2.7 Transient thermal conductivity analysis

Fig. 11 represents the transient thermal conductivity of all four FTEGs at varying temperatures calculated using the Weide-mann–Franz equation shown in eqn (4).

$$K = L\sigma T \tag{4}$$

where L is the Lorentz number, σ is the electrical conductivity, and T is the absolute temperature. It exhibits a linear trend with increasing temperature, suggesting heat transport mechanisms within the materials. Among the four samples, PI exhibits the lowest transient thermal conductivity value of 0.2×10^{-5} W $m^{-1}\ K^{-1}$ at 368 K. As the temperature rises further, more continuous thermal conduction pathways may form, leading to the observed increase in conductivity at higher temperatures.[54]

High carrier concentration and low electron mobility can lead to increased thermal conductivity. Consequently, ZPI-5 exhibits a similar trend, with consistently higher thermal conductivity values of up to 0.6×10^{-5} W $m^{-1}\ K^{-1}$, compared

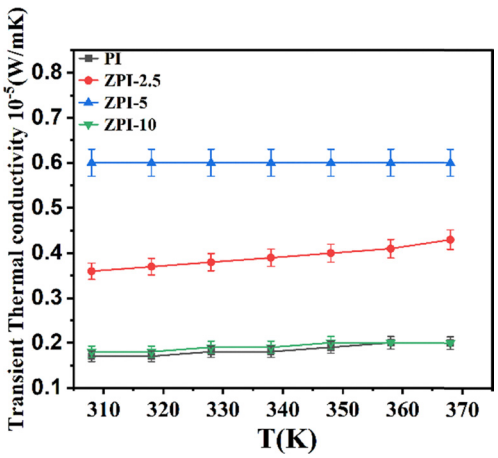

Fig. 11 Transient thermal conductivity of PPy and ZPI-based FTEGs.

to the other FTEGs. This can be attributed to the pore blocking and the resulting decrease in phonon scattering. In contrast, ZPI-10 displays lower thermal conductivities across all temperatures. The increased thermal conductivity of the screen-printed films is due to PPy effectively filling or blocking the pores within the ZIF-67 framework. The SEM, BET, and thermal measurements reveal a clear correlation between morphology, pore structure, and thermal transport of the materials. The transition from a highly porous ZIF-67 framework to a PPy-coated composite decreases pore scattering and improves interfacial contact between the two phases. This structural modification enables more effective phonon transport, leading to increased thermal conductivity. Therefore, the combined effects of reduced porosity, stronger interfacial bonding, and rough surface morphology contribute to the enhanced thermal transport and observed increase in thermal conductivity. This may be related to the decrease in mobility and increase in carrier concentration.[55] Additionally, incorporating cellulose acetate binder into the ZIF-67/PPy matrix promotes charge carrier scattering and helps to reduce thermal conductivity.[24]

2.8 Temperature-dependent voltage and resistance analysis

The thermoelectric behaviour of the ink-based samples was evaluated by analysing their resistivity and voltage response as a function of the temperature gradient (ΔT). The resistivity graph in Fig. 12(a) shows that PI exhibits the highest resistivity across the entire ΔT range, starting at 23.94 kΩ and gradually decreasing as the temperature increases. In contrast, the ZP ink-based samples (ZPI-2.5, ZPI-5, and ZPI-10) exhibited significantly lower resistivity values, while the resistivities of ZPI-5 and ZPI-10 were the lowest, between 5 to 6 kΩ. According to the relation ($\sigma = 1/\rho$), the FTEG with the highest electrical conductivity exhibits the lowest resistivity. Declined resistivity indicates an improvement in the thermoelectric performances of the FTEGs due to the enhancement in the concentration of the charge carriers and electrical conductivity.

Fig. 12(b) shows the increasing voltage output of the ink-based samples with the applied temperature gradient (ΔT). This trend is consistent with the Seebeck effect, which describes the generation of voltage due to a thermal gradient across a conductive material.

Among the tested samples, ZPI-5 reached the highest voltage output of 1.7 mV at ΔT = 95 °C, while ZPI-2.5 reached the lowest, showing a voltage output of 1.2 mV over the same range. All the findings indicate that the ZPI-5 ink-based FTEG significantly improves the thermoelectric performance by simultaneously reducing resistivity and enhancing the Seebeck voltage generation.

2.9 Thermoelectric analysis

The thermoelectric performances of the FTEGs were evaluated based on their Seebeck coefficient (S) along with their power output (PO), power factor (PF), and power density (P_d) with respect to the temperature gradient as depicted in Fig. 13. The Seebeck coefficient is calculated using eqn (5). All ink-based FTEGs showed linear plots, indicating p-type behaviour with positive thermopower.

$$S = \frac{\Delta V}{\Delta T} \tag{5}$$

where ΔV and ΔT are the voltage and temperature differences, respectively.

Among the various compositions, the ZPI-5 sample exhibited the highest Seebeck coefficient of 16.17 μV K^{-1}, surpassing that of PI, which is 13.87 μV K^{-1}. This enhancement can be attributed to the reduction in the electrical resistivity with no hindrance in the charge transport.[56] However, when the filler content exceeds the optimal level as observed in ZPI-10, the Seebeck coefficient decreases back to 13.63 μV K^{-1}. This decline is due to an excessive reduction in efficiency in charge carrier transport and low voltage at all ΔT (Fig. 12(b)).

Fig. 13(b) provides the power output of the fabricated FTEGs at different temperature gradients ΔT. FTEGs with higher Seebeck coefficients exhibit greater power output. The power output (P) is calculated using eqn (6):

$$P = \frac{V^2}{R} \tag{6}$$

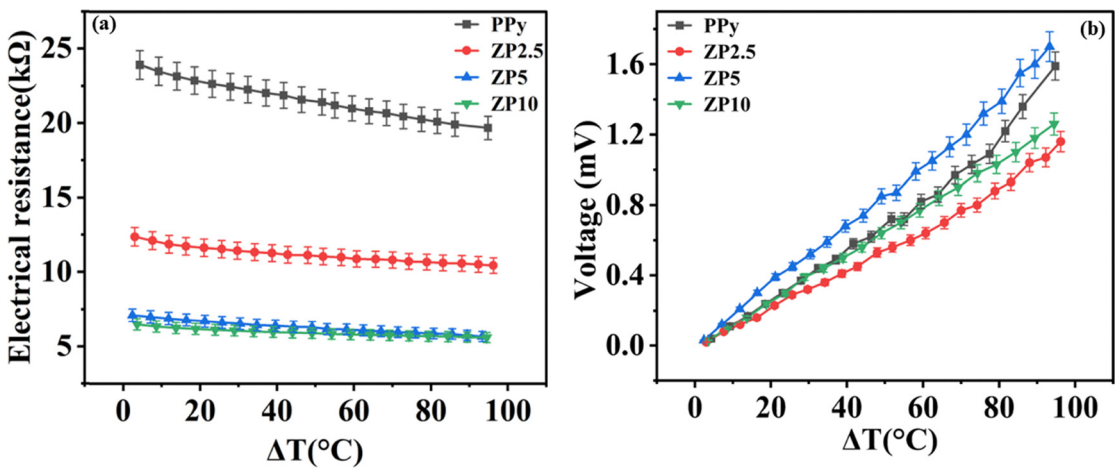

Fig. 12 (a) Resistivity *vs.* ΔT and (b) ΔV *vs.* ΔT curves of ink-based FTEGs.

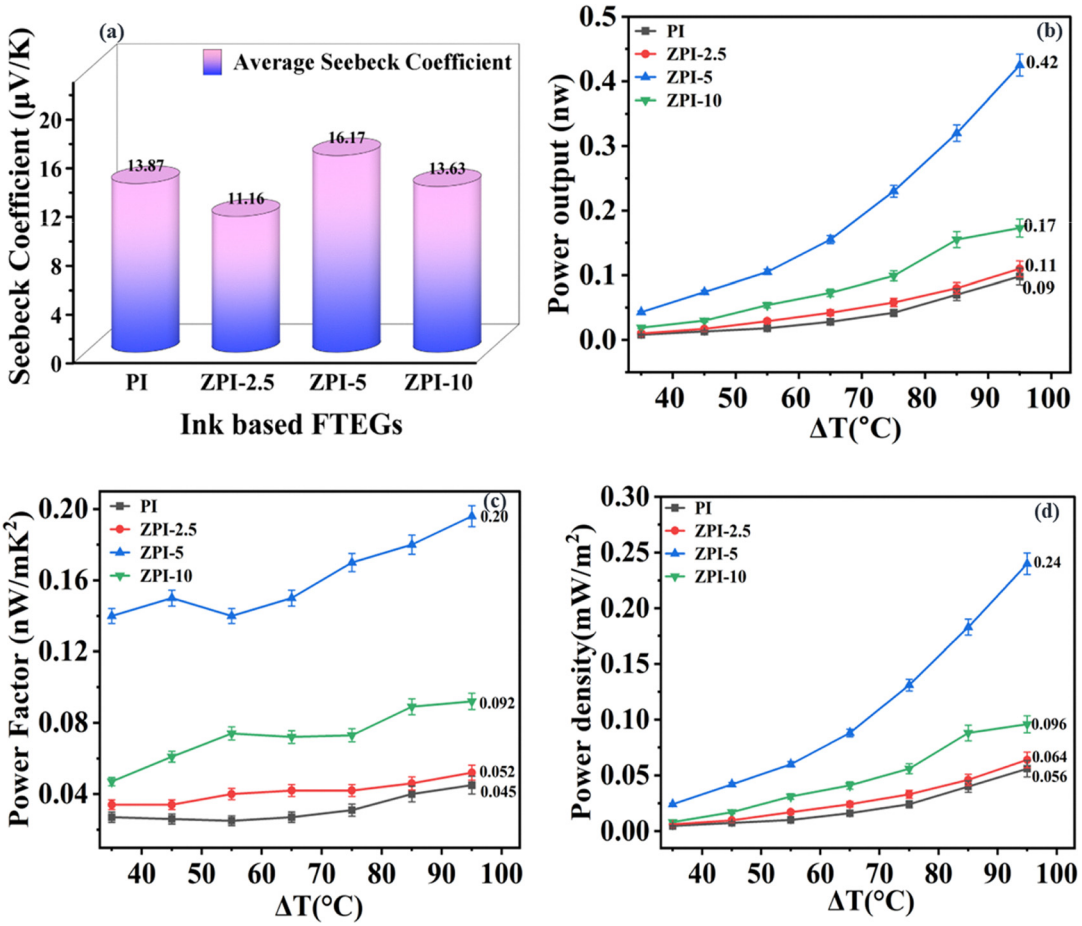

Fig. 13 Comparison of (a) Seebeck coefficient, (b) power output, (c) power factor and (d) power density of ink-based FTEGs.

where V is the voltage applied and R is the resistance in ohms. PI exhibits a reduced power output of 0.09 nW, which consequently lowers both its power factor and power density. A maximum power output of 0.42 nW was obtained for the ZPI-5 ink-based FTEG because of its high Seebeck coefficient, as shown in Fig. 13(a). Furthermore, a comparison of the FTEGs clearly shows that the incorporation of ZIF-67 significantly enhances the power output efficiency, demonstrating the beneficial role of the filler in improving thermoelectric performance. The power factor (PF), which reflects a material's thermoelectric efficiency, depends on both the Seebeck coefficient and electrical conductivity.[57] It was calculated using eqn (7)

$$\text{Power factor} = \frac{\text{PO}}{A \times \Delta T^2} \tag{7}$$

where PO is the maximum power output, A is the area of the FTEG, and ΔT is the maximum temperature gradient.

The highest PF value of 0.20 nW m^{-1} K^{-2} was recorded for ZPI-5 (containing 5 wt% ZIF-67) at a temperature gradient of 95 °C. In contrast, the PF values calculated for PI, ZPI-2.5, and ZPI-10 were 0.045, 0.052, and 0.045 nW m^{-1} K^{-2}, as shown in Fig. 13(c), respectively. These results highlight that the power factor of ZPI-5 FTEG is 5.33 times higher than that of PPy.

The power density (P_d) of the FTEGs was calculated using eqn (8)

$$P_d = \frac{\text{PO}}{N \times A} \tag{8}$$

where PO is the maximum power output in nW, N is the number of TE legs of the FTEG, and A is the cross-sectional area of the TE legs in m^2. Since the power density depends on the power output, the power density of 0.24 mW m^{-2} was obtained for ZPI-5, which is 328.6% higher than the pristine PPy-based device, as shown in Fig. 10(d). For PI, ZPI-2.5, and ZPI-10, the density values were 0.056, 0.064, and 0.056 mW m^{-2}, respectively, at a temperature gradient of 95 °C.

The ZPI-5 exhibited a clear decoupling of electrical and thermal transport through the interplay of electrical conductivity (σ), Seebeck coefficient (S), and transient thermal conductivity (κ), as supported by its measured transport properties (Fig. 10, 11 and 13). The ZPI-5 ink based FTEG shows an electrical conductivity of 0.81 S m^{-1} and a Seebeck coefficient of 16.17 μV K^{-1}, resulting in a power factor of 0.21 nW m^{-1} K^{-2} and power output of 0.42 nW. Using the Wiedemann Franz relation, the electronic thermal conductivity is estimated to be 6×10^{-6} W m^{-1} K^{-1}, which is negligible compared to the total thermal conductivity of approximately 0.20 W m^{-1} K^{-1}.

Although the lattice thermal conductivity could not be directly measured due to limited experimental facilities, it can reasonably be inferred to be low. As previously reported by Sunmi Shin,[58] the incorporation of the binder through the screen printing method effectively reduces the lattice thermal conductivity by generating defect sites that serve as phonon-scattering centers, thereby suppressing lattice heat transport. Similarly, we assume that in the ZPI-5 composite based FTEG, the bio-based binder partially decomposes during the printing and drying processes along with the solvent evaporation, leaving behind nanoscale voids (Fig. 15) and defect structures that hinder phonon propagation while maintaining efficient charge transport through interconnected PPy domains. Consequently, the minimal increase in thermal conductivity relative to electrical conductivity confirms an effective decoupling of electrical and thermal transport.

Due to the better power output performance of the ZPI-5 ink-based FTEG, it was taken for analysis through its voltage–current (V–I) characteristics and power output response. The V–I curves recorded from 25 °C to 85 °C show linear relationships, indicating stable internal resistance across the operating range. At 85 °C, the open-circuit voltages reach nearly 1.0 mV compared to 0.25 mV at 25 °C, demonstrating that a higher temperature gradient enhances voltage generation. Further performance evaluation was conducted under different load resistances (0 to 15 kΩ). As illustrated in Fig. 14(a) and (b), the voltage and power outputs were measured at five different temperature gradients (ΔT = 25, 30, 50, 65, and 85 °C). The results show that both voltage and power output increased with ΔT, while the internal current gradually decreased. In line with the maximum power transfer principle, the highest power output was achieved when the external load resistance matched the internal resistance of the flexible thermoelectric generator.[59] Maximum power values for each temperature gradient were calculated using eqn (9).[33]

$$P_{max} = \frac{V_L^2}{4R_L} \quad (9)$$

where P_{max} is the maximum power output (W), V_L is the output voltage (V) across the load, and R_L is the load resistance (Ω).

2.10 SEM analysis of FTEGs

Fig. 15(a) and (b) illustrate the surface area and cross-sectional morphologies of the screen-printed PI and ZPI-5. The PI sample exhibits a rough, granular texture with densely packed particles, indicating PPy agglomeration. The ZPI-5 structure exhibits irregular morphology with reduced porosity, characterized by surface roughness and a large, interconnected framework of densely packed particles. Repeated overprinting of crystalline particles results in a reduction in the sample's porosity. Cross-sectional images shown in Fig. 15(c) and (d) further substantiate the observed differences. The thickness of the PI film ranges from 29 to 35 μm, whereas the ZPI-5 film exhibits a thickness between 35 and 41 μm, characterized by a more heterogeneous, multilayered architecture.

2.11 Rheological analysis of the ink

The viscosity behavior of the ink was studied for two different temperatures (25 and 45 °C) as shown in Fig. 16(a) and (b). The viscosity plot demonstrates a shear-thinning behavior, *i.e.*, viscosity decreases as shear rate increases, as shown in Fig. 16(a). This behavior is typical for non-Newtonian fluids, especially conductive polymer-based inks used for screen-printing.

At 25 °C, the ink exhibits its highest viscosity, nearly 7000 cP at low shear rates, indicating a strong internal network that resists flow. As the temperature increases to 45 °C, viscosity decreases significantly, suggesting improved flow properties. This reduction in viscosity is crucial for achieving uniform and consistent printing.[60] The reduction in viscosity with increasing temperature is attributed to weakened intermolecular interactions within the ink formulation, which enhances its spreadability during printing. At 45 °C, the ink maintains a stable rheological profile, demonstrating suitability for screen-printing processes. These results indicate that elevated

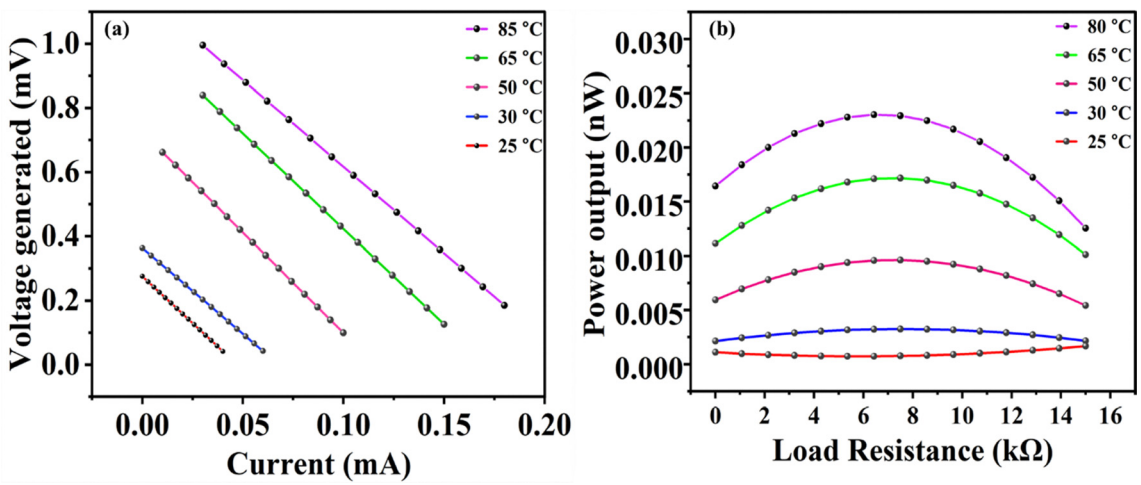

Fig. 14 Comparison of (a) current–voltage and (b) power output *vs.* load resistance of the ZPI-5 ink-based FTEG.

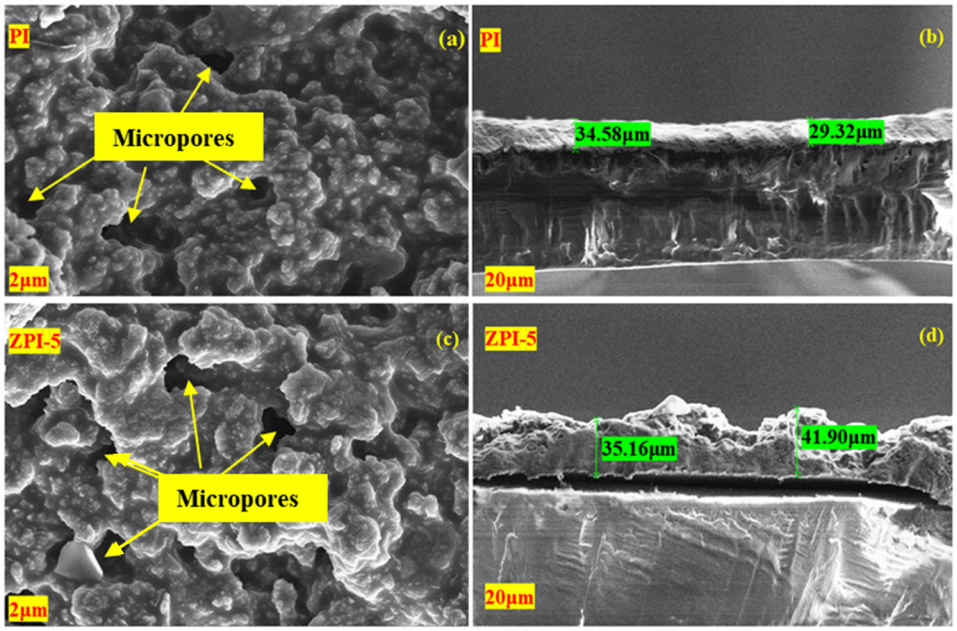

Fig. 15 SEM images of (a) PI, (b) cross-section of PI-based FTEG, (c) ZPI-5, and (d) cross-section of ZPI-5-based FTEG.

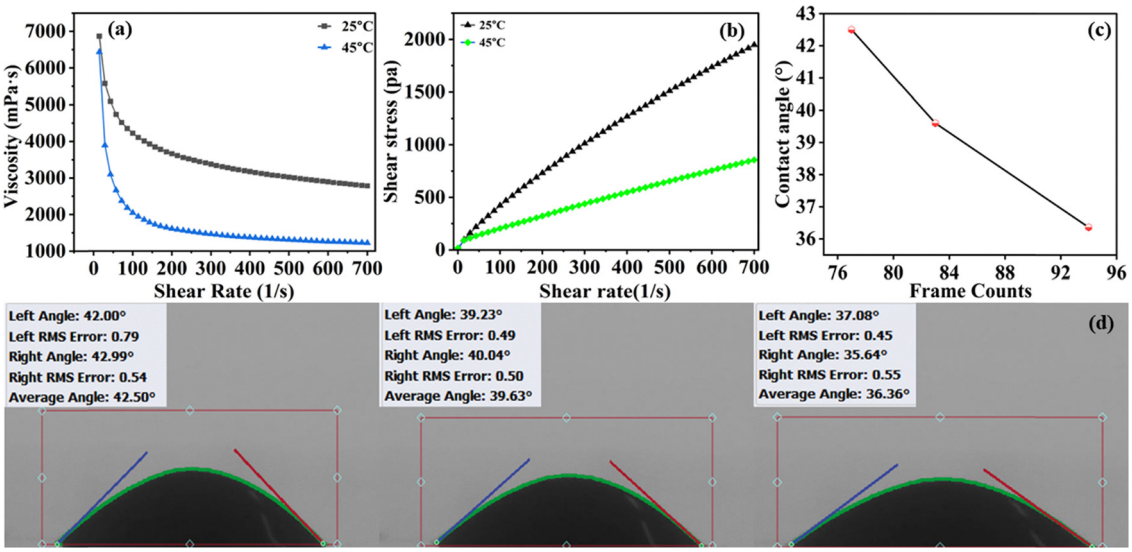

Fig. 16 Rheological behaviour of the ZPI-5 ink: (a) viscosity *vs.* shear rate, (b) shear stress *vs.* shear rate, (c) contact angle *vs.* frame count and (d) contact angle with different frame counts.

temperatures improve ink processability, making it more adaptable for the fabrication of flexible thermoelectric generators.[61]

The rheological behaviour of ZPI-5 ink, as depicted in the shear stress *versus* shear rate graph in Fig. 16(b), demonstrates a distinct temperature-dependent viscosity profile characteristic of non-Newtonian fluids. Across the tested temperature range, the shear stress increases with shear rate, indicating shear thinning behavior where viscosity decreases as shear rate increases. Notably, the shear stress is highest at 25 °C and decreases progressively with rising temperatures. At 25 °C, the ink exhibits the highest resistance to flow, reaching a shear stress of over 2000 Pa at a shear rate of 700 s^{-1}. In contrast, at 45 °C, the maximum shear stresses are significantly lower, with values falling to around 1000 Pa. This trend highlights the critical role of temperature in modulating the viscosity of ZPI-5 ink, likely due to weakened intermolecular interactions and improved fluidity at elevated temperatures.[62]

Fig. 16(c) illustrates the variation in the contact angle of ZPI-5 ink over a series of frame counts, reflecting temporal changes or progression in the printing process, and Fig. 13(d) shows the images of the contact angle with different frame counts. At the initial frame count of 77, the contact angle is 42.5°, indicating a

relatively high wettability resistance. As the frame count increases to 83, the contact angle drops significantly to around 39.3° and continues to decline to 36.2° at a frame count of 94. This consistent downward trend demonstrates that the contact angle of the ZPI-5 ink decreases with increasing frame counts, suggesting that the ink is progressively spreading or wetting the surface more effectively over time.[63] This behaviour might be indicative of enhanced adhesion or spreading dynamics of the ink as it interacts with the substrate. This suggests a favourable interaction between the ink and the substrate, which ensures consistency during the printing or coating process.[64]

2.12 Optical and FTIR ink analysis

The energy band gap of the composites shown in Fig. 8 was calculated from the reflectance obtained from the Tauc plot, providing a comparative optical characterization of ZIF-67, PPy, ZP5, PI, and ZPI-5. Among the samples, ZIF-67 shows a relatively sharp absorption edge near 2.03 eV, signifying the widest band gap among all the samples.[65] In contrast, PPy, ZP5, ZPI-5, and PI show earlier absorption edges, indicating narrower band gaps. Since ZP5 is the optimized concentration exhibiting good power factor and Seebeck coefficient (Fig. 13), it exhibits a steep rise in absorption beginning near 1.4 eV, suggesting a direct optical band gap of approximately 1.43 eV, as indicated on the graph. After the addition of PPy, the band gap of ZIF-67 is found to decrease, highlighting its improved conductivity.

In the PI and ZPI composites, as shown in Fig. 17(b), the broad band at 3450 cm^{-1} corresponds to O–H stretching, while the peaks around 2921–2924 cm^{-1} are attributed to C–H stretching vibrations. The vibrations at 1642, 1460–1467, and 1125 cm^{-1} arise from overlapping C=N stretching and imidazole rings with PPy ring vibrations. The Co–N vibration found at 423 cm^{-1} confirms the successful incorporation of the cobalt-imidazole framework into the PPy matrix. Additional skeletal vibrations of PPy are observed at 1031, 782, and 616 cm^{-1}, showing slight shifts that suggest structural interaction within the composite.[66]

2.13 Thermoelectric analysis of p–n type devices

A p–n type FTEG was fabricated using ZPI-5 as the p-type and MnO_2 as the n-type leg to analyse its performance. MnO_2, a promising n-type thermoelectric material[26] showed a Seebeck coefficient of 171.6 μV K^{-1} at 368 K, as shown in Fig. 18(a), which indicates a strong voltage generation in response to the temperature gradient. This value suggests good compatibility between the two materials for thermoelectric use.

A power output of 26 nW, a power factor of 12 nW m^{-1} K^{-2}, and a power density of 14.8 mW m^{-2} were exhibited by the p–n type FTEG, at the temperature gradient of 95 °C, as shown in Fig. 18(b)–(d). These results show that the ZPI-5-MnO_2 combination is effective in converting heat into electricity in a printed format. In comparison with traditional materials like Bi_2Te_3, CNTs, and SnTe, our FTEG exhibits a lower output.[67] However, we have approached and presented a method to improve the TE properties by integrating ZIF-67 and PPy materials. The combination of these materials provides a good balance of Seebeck coefficient and power output, making them suitable for low-temperature thermoelectric applications. Table 4 depicts the comparison of the thermoelectric performance of the ZIF-67/PPy printed TEG with previously reported TEGs.

2.14 Bending test analysis

Fig. 19(a) shows the bending analysis of the printed FTEGs based on PI, ZPI-5, and ZPI-5 & MnO_2, performed using a customized setup.[33] The variation in internal resistance of the FTEGs, concerning demonstrated higher thermoelectric efficiency than the other FTEGs, the bending angle of ZPI-5 was calculated. The bending test shows that the resistance of all the FTEGs increases linearly with the bending angle. The variation remains small, not

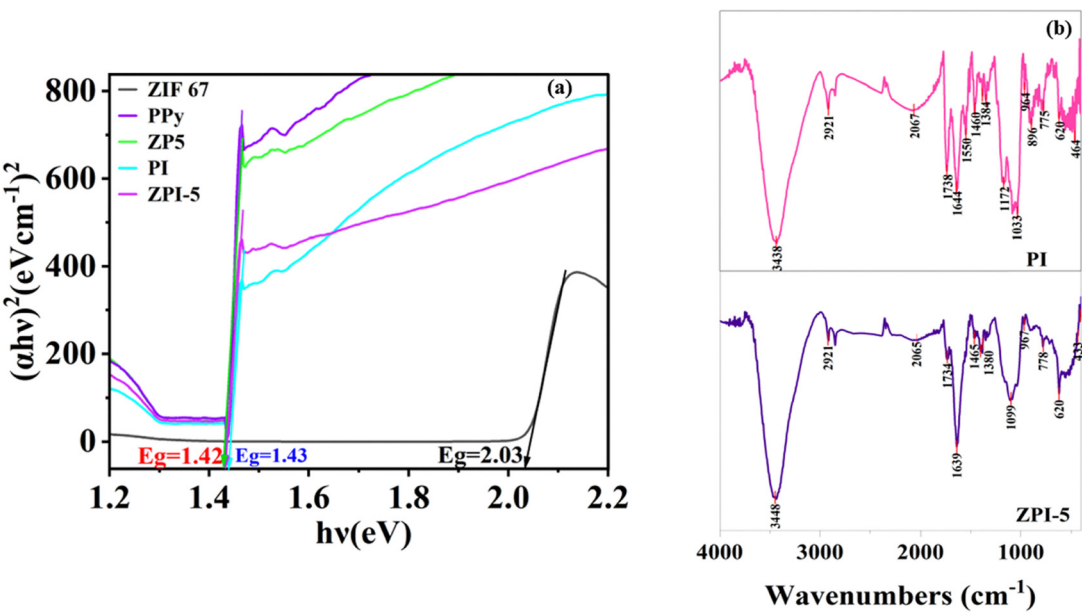

Fig. 17 (a) Tauc plot and optical bandgap of the composites and inks. (b) FTIR spectra of the PI and ZPI-5 ink composites.

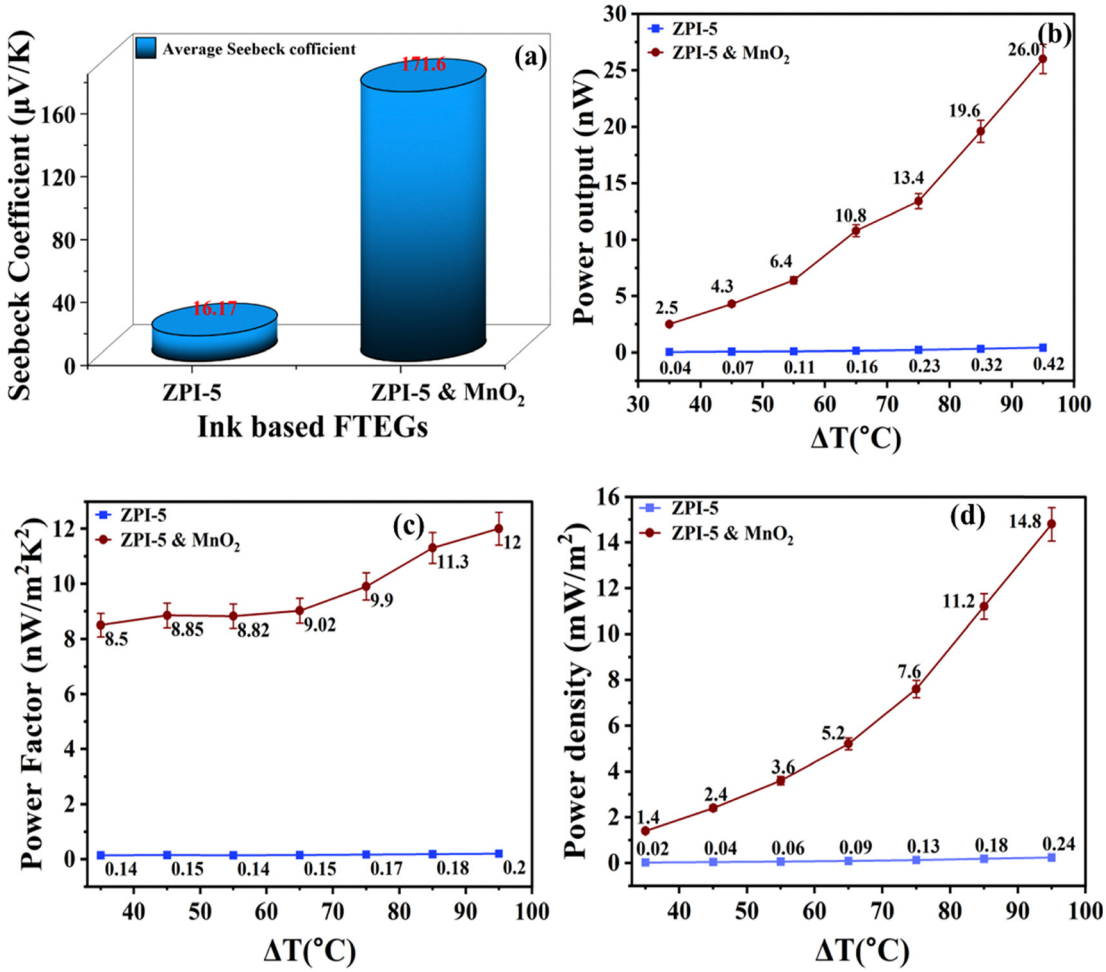

Fig. 18 Comparison of (a) Seebeck coefficient, (b) power output, (c) power factor, and (d) power density between ZPI-5 and ZPI-5 & MnO_2 FTEGs.

Table 4 Comparison of the thermoelectric performance of the ZIF-67/PPy printed TEG with previously reported TEGs

Materials	Substrate	Fabrication method	Seebeck coefficient (μV K^{-1})	Power output (nW)	Ref. #
PPy–Ag nanoparticles	BOPET	Dip coating	12.0	0.03	68
Bi_2Te_3/GeTe	Polyimide	Physical vapour deposition	140	0.4	69
WS_2/$NbSe_2$	PDMS	Printing	75 and 14	0.63	70
PANI/graphite	PET	Screen printing	22.51	0.002	53
MWCNT/Fe_2O_3	PET	Screen printing	43.37	0.32	71
PANI/graphite/Bi_2Te_3 composite	PET	Screen printing	39.14	0.58	72
Bi_2Te_3–Ga_2Te_3	—	Induction melting	158.72	—	73
Bi_2Te_3 nanoplates/SWCNTs	—	Wet	−37	—	74
Bi_2Te_3 nanoplates/SWCNTs (top)	Polyimide sheet	Wet	−131	—	75
Bi_2Te_3 nanoplates/SWCNTs (bott)	Polyimide sheet	Wet	−118	—	75
ZIF-67/PPy	PET	Screen printing (p-type)	16.17	0.42	[a]
ZIF-67/PPy/MnO_2	PET	Screen printing (p–n type)	171.6	22.6	[a]

[a] Present work.

exceeding 4% more than the original resistance. Even though PPy has film forming properties, the ability of the polymer to deform during bending and the use of an insulating binder is responsible for increase in FTEG resistivity. However, the percentage in resistance is less than for materials fabricated using film casting[76] and magnetron sputtering,[77] indicating good mechanical flexibility. Fig. 19(b) shows the bending cycle test, carried out up to 1000 cycles, which showed that the resistance of all FTEGs increased linearly with repeated bending, yet stayed within 5% of the initial value. This outcome highlights strong mechanical stability, confirming their suitability for use in wearable devices.

The ZPI-5 composite exhibits good mechanical flexibility compared to PI and ZPI-5 & MnO_2, further maintaining a nearly constant low resistance throughout bending, demonstrating

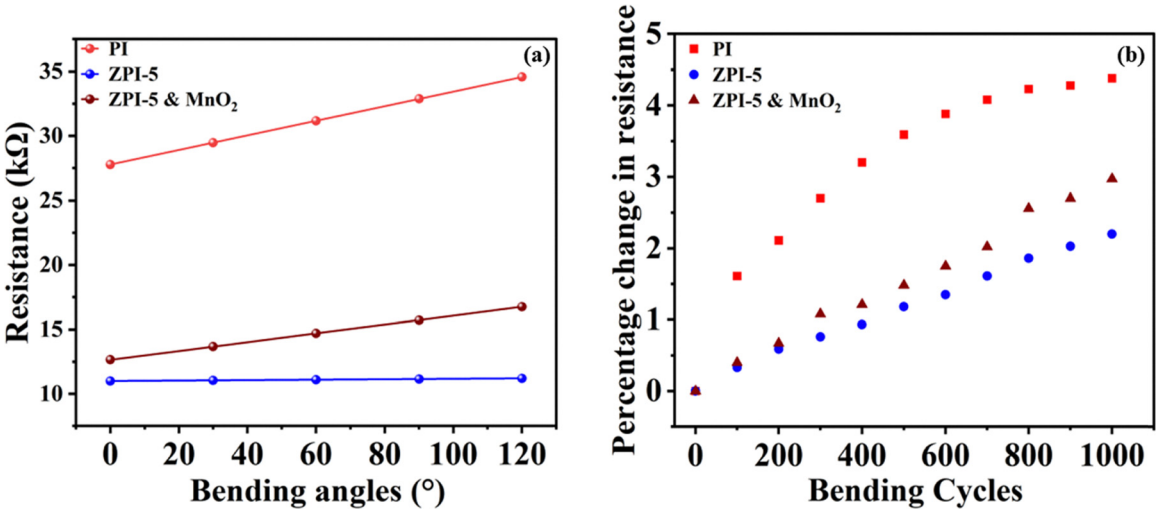

Fig. 19 (a) Resistance variation with the bending angles and (b) percentage change in resistance with the bending cycles of FTEGs.

superior structural stability. The minimal change in resistance of ZPI-5 suggests enhanced mechanical robustness due to the incorporation of ZIF-67.

3. Conclusions

In this study, ZIF-67 was successfully incorporated into a PPy matrix to fabricate a series of conductive composites for thermoelectric applications. The dispersion of ZIF-67 within the PPy framework introduces enhanced structural stability, improved charge transport pathways, and optimized porosity, leading to significant improvements in functional performance. Comprehensive characterization through XRD, SEM, XPS, FTIR, and UV-vis spectroscopy confirmed the successful embedding of ZIF-67 within the PPy network and revealed synergistic interactions between ZIF-67 and the conductive polymer matrix. ZPI-5 exhibited the best balance between electrical conductivity, mechanical integrity, and thermoelectric response among these compositions. ZPI-5 FTEG exhibited 328.6% higher power density than the PPy-based FTEG along with a Seebeck coefficient of 16.17 μV K^{-1} and a power output of 0.42 nW m^{-1} K^{-2} at 95 °C. Additionally, a ZPI-5 & MnO_2 based p–n type FTEG exhibited a Seebeck coefficient of 171.6 μV K^{-1}, power output of 26 nW, and power factor of 12 nW m^{-2} K^{-2} at a temperature gradient of 95 °C. These results underline the material's potential for converting low-grade thermal energy into electrical energy, particularly in wearable and flexible electronics, where lightweight and adaptable materials are essential. Overall, this study highlights the effectiveness of embedding metal–organic frameworks like ZIF-67 into conductive polymers, offering a versatile strategy to multifunctional materials for next-generation energy and sensing technologies.

Author contributions

Kishor D Kalarakoppa: writing – original draft, methodology, and investigation. A N Prabhu: writing – review and editing, conceptualization and resources. Ramakrishan Nayak: writing – review and editing, methodology, and resources. Nishitha Prabhu: resource and investigation. Mohammad Saquib: resource and investigation. Shilpa Shetty: resource and investigation. Kavya Naik: resource and investigation.

Conflicts of interest

The authors declare that they have no known competing financial interests or personal relationships that could have appeared to influence the work reported in this paper.

Data availability

The data that support the findings of this study are available from the corresponding author, (A N Prabhu), upon reasonable request.

Acknowledgements

This research did not receive any specific grant from funding agencies in the public, commercial, or not-for-profit sectors. The authors would like to express their sincere gratitude to the Manipal Institute of Technology, MAHE, for providing financial assistance through the Dr T. M. A. Pai doctoral fellowship and the laboratory facilities to carry out this research work.

References

1 L. Yan, M. Shao, H. Wang, D. Dudis, A. Urbas and B. Hu, High seebeck effects from hybrid metal/polymer/metal thin-film devices, *Adv. Mater.*, 2011, **23**(35), 4120–4124.
2 N. Jaziri, A. Boughamoura, J. Müller, B. Mezghani, F. Tounsi and M. Ismail, A comprehensive review of Thermoelectric Generators: Technologies and common applications, *Energy Rep.*, 2020, **6**, 264–287.

3 M. A. Gordillo, P. A. Benavides, K. Ma and S. Saha, Transforming an Insulating Metal-Organic Framework (MOF) into Semiconducting MOF/Gold Nanoparticle (AuNP) and MOF/Polymer/AuNP Composites to Gain Electrical Conductivity, *ACS Appl. Nano Mater.*, 2022, **5**, 13912–13920.
4 B. Dhara, S. S. Nagarkar, J. Kumar, V. Kumar, P. K. Jha and S. K. Ghosh, *et al.*, Increase in Electrical Conductivity of MOF to Billion-Fold upon Filling the Nanochannels with Conducting Polymer, *J. Phys. Chem. Lett.*, 2016, **7**(15), 2945–2950.
5 W. Dou, Y. Gong, X. Huang, Y. Li, Q. Zhang and Y. Liu, *et al.*, CdSe Quantum Dots Enable High Thermoelectric Performance in Solution-Processed Polycrystalline SnSe, *Small*, 2024, **20**(28), 2311153, DOI: 10.1002/smll.202311153.
6 X. Qian, H. Wu, D. Wang, Y. Zhang, J. Wang and G. Wang, *et al.*, Synergistically optimizing interdependent thermoelectric parameters of n-type PbSe through alloying CdSe, *Energy Environ. Sci.*, 2019, **12**(6), 1969–1978.
7 A. Babu, L. Bochu, S. Potu, R. Kaja, N. Madathil and M. Velpula, *et al.*, Facile Direct Growth of ZIF-67 Metal-Organic Framework for Triboelectric Nanogenerators and Their Application in the Internet of Vehicles. ACS Sustain, *Chem. Eng.*, 2023, **11**(47), 16806–16817.
8 L. K. Allison and T. L. Andrew, A Wearable All-Fabric Thermoelectric Generator, *Adv. Mater. Technol.*, 2019, **4**(5), 1800615, DOI: 10.1002/admt.201800615.
9 D. Kong, W. Zhu, Z. Guo and Y. Deng, High-performance flexible Bi_2Te_3 films based wearable thermoelectric generator for energy harvesting, *Energy*, 2019, **175**, 292–299.
10 B. S. Haile, V. Pal, T. Pal, S. Slathia, G. M. Jigi and S. D. Negedu, *et al.*, Direct Ink Writing (3D Printing) of Robust, Highly Efficient, Double-Half-Heusler Thermoelectric High-Entropy Alloy, *Adv. Eng. Mater.*, 2025, **27**(7), 2402283, DOI: 10.1002/adem.202402283.
11 A. K. Singh, R. Karthik, P. R. Sreeram, T. K. Kundu and C. S. Tiwary, Enhanced Thermoelectric Performance of Nanostructured 2D Tin Telluride, *Small*, 2024, **20**(43), 2403728, DOI: 10.1002/smll.202403728.
12 R. Li, B. Ge and C. Zhou, Advanced porous thermoelectric materials: Design, construction, and application, *Nano Res.*, 2025, **18**(4), 94907308, DOI: 10.26599/NR.2025.94907308.
13 U. Ijaz, M. Siyar and C. Park, The power of pores: review on porous thermoelectric materials, *RSC Sustainability*, 2024, **2**, 852–870.
14 R. Ahmad, U. A. Khan, N. Iqbal and T. Noor, Zeolitic imidazolate framework (ZIF)-derived porous carbon materials for supercapacitors: an overview, *RSC Adv.*, 2020, **10**, 43733–43750.
15 S. Kouser, A. Hezam, M. J. N. Khadri and S. A. Khanum, A review on zeolite imidazole frameworks: synthesis, properties, and applications, *J. Porous Mater.*, 2022, **29**(3), 663–681.
16 X. Yuan, Q. Mu, S. Xue, Y. Su, Y. Zhu and H. Sun, *et al.*, Polypyrrole reinforced ZIF-67 with modulated facet exposure and billion-fold electrical conductivity enhancement towards robust photocatalytic CO_2 reduction, *J. Energy Chem.*, 2021, **60**, 202–208.
17 P. S. Chang and C. N. Liao, Screen-printed flexible thermoelectric generator with directional heat collection design, *J. Alloys Compd.*, 2020, 836.
18 A. Ebrahim, M. Ghali and A. A. El-Moneim, Microporous Zr-metal-organic frameworks based-nanocomposites for thermoelectric applications, *Sci. Rep.*, 2024, **14**(1), 13067, DOI: 10.1038/s41598-024-62317-3.
19 W. Xu, Y. Zhao, H. Wang, H. Wang, F. Pan and R. Xu, *et al.*, Postsynthetic-Modified PANI/MOF Composites with Tunable Thermoelectric and Photoelectric Properties, *Chem. – Eur. J.*, 2021, **27**(15), 5011–5018.
20 M. H. Lin, C. H. Hsu, D. Y. Kang and C. L. Liu, Correlating framework structures and thermoelectric performance of metal–organic framework/carbon nanotube thermoelectric hybrids with n–p type inversion, *Chem. Eng. J.*, 2024, **485**, 149732, DOI: 10.1016/j.cej.2024.149732.
21 M. Saquib, R. Nayak, D. Devadiga, M. Selvakumar, S. Paramasivam and C. Ghosh, *et al.*, Printed flexible supercapacitor from conductive ink of graphite nanocomposite blended with Co_3O_4 to facilitate the fabrication of energy storage device, *J. Energy Storage*, 2023, **72**, 108800, DOI: 10.1016/j.est.2023.108800.
22 A. Babu, L. Bochu, S. Potu, R. Kaja, N. Madathil and M. Velpula, *et al.*, Facile Direct Growth of ZIF-67 Metal-Organic Framework for Triboelectric Nanogenerators and Their Application in the Internet of Vehicles, *ACS Sustainable Chem. Eng.*, 2023, **11**(47), 16806–16817.
23 A. Babu, K. Ruthvik, P. Supraja, M. Navaneeth, K. U. Kumar and R. R. Kumar, *et al.*, High-performance triboelectric nanogenerator using ZIF-67/PVDF hybrid film for energy harvesting, *J. Mater. Sci.: Mater. Electron.*, 2023, **34**(33), 2195, DOI: 10.1007/s10854-023-11644-8.
24 R. Nayak, P. Shetty, M. Selvakumar, A. Rao and K. M. Rao, Formulation of new screen printable PANI and PANI/Graphite based inks: printing and characterization of flexible thermoelectric generators, *Energy*, 2022, **238**, 121680, DOI: 10.1016/j.energy.2021.121680.
25 M. H. Memon, U. E. S. Amjad, A. Mir and M. Mustafa, ZIF-67-Based Triboelectric Nanogenerator Fabricated Through EHD Printing: Performance Evaluation as an Energy Harvesting Device and Its Pressure-Sensing Application, *ACS Appl. Electron Mater.*, 2024, **6**(4), 2178–2187.
26 M. R. Shankar, A. N. Prabhu, R. Nayak and M. Saquib, Optimization of thermoelectric parameters in Ag/MnO_2 nanocomposite-based flexible thermoelectric generators, *Ceram. Interfaces*, 2025, **51**(9), 11821–11833, DOI: 10.1016/j.ceramint.2025.01.035.
27 X. Guo, T. Xing, Y. Lou and J. Chen, Controlling ZIF-67 crystals formation through various cobalt sources in aqueous solution, *J. Solid State Chem.*, 2016, **235**, 107–112.
28 B. Habibi, Y. Bahadori, S. Pashazadeh and A. Pashazadeh, ZIF-67 decorated with silica nanoparticles and graphene oxide nanosheets composite modified electrode for simultaneous determination of paracetamol and diclofenac, *Sci. Rep.*, 2025, **15**(1), 9499, DOI: 10.1038/s41598-025-94178-9.

29 R. Singaravelan and S. B. S. Alwar, Effect of reaction parameters in synthesis, characterisation of electrodeposited zinc nanohexagons, *J. Nanostruct. Chem.*, 2014, **4**(4), 109–117.
30 M. U. Shariq, A. Husain, M. Khan and A. Ahmad, Synthesis and characterization of polypyrrole/molybdenum oxide composite for ammonia vapour sensing at room temperature, *Polym. Polym. Compos.*, 2021, **29**(9_suppl), S989–S999.
31 V. D. Thao, B. L. Giang and T. V. Thu, Free-standing polypyrrole/polyaniline composite film fabricated by interfacial polymerization at the vapor/liquid interface for enhanced hexavalent chromium adsorption, *RSC Adv.*, 2019, **9**(10), 5445–5452.
32 R. Matsumoto, Y. Hoshina and N. Akuzawa, Thermoelectric properties and electrical transport of graphite intercalation compounds, *Mater. Trans.*, 2009, **50**(7), 1607–1611.
33 R. Nayak, A. Sudhakaran Nair, P. Shetty, M. Selvakumar, A. Rao and A. Kompa, *et al.*, Effect of graphite on the power density of selenium doped polyaniline ink based hybrid screen-printed flexible thermoelectric generator, *Ceram. Interfaces*, 2023, **49**(13), 21767–21776, DOI: 10.1016/j.ceramint.2023.03.318.
34 W. Sun, X. Zhai and L. Zhao, Synthesis of ZIF-8 and ZIF-67 nanocrystals with well-controllable size distribution through reverse microemulsions, *Chem. Eng. J.*, 2016, **289**, 59–64.
35 M. A. Chougule, S. G. Pawar, P. R. Godse, R. N. Mulik, S. Sen and V. B. Patil, Synthesis and Characterization of Polypyrrole (PPy) Thin Films, *Soft Nanosci. Lett.*, 2011, **01**(01), 6–10.
36 X. Xu, J. Tang, H. Qian, S. Hou, Y. Bando and M. S. A. Hossain, *et al.*, Three-Dimensional Networked Metal-Organic Frameworks with Conductive Polypyrrole Tubes for Flexible Supercapacitors, *ACS Appl. Mater. Interfaces*, 2017, **9**(44), 38737–38744.
37 L. Jiang, M. Xu, M. Bao, Y. Dong, Y. Yuan and X. Zhou, *et al.*, Electrodeposited ZIF-67 reinforced polypyrrole coating on ferritic stainless steel substrate with durable anticorrosion performance, *Mater. Today Chem.*, 2024, **38**, 102084, DOI: 10.1016/j.mtchem.2024.102084.
38 J. Zhao, Air-Flow Impacting: A New Mechanochemical Method for Continuous, Highly Efficient, Large-Scale Synthesis of Metal–Organic Frameworks and Mechanistic Research, *Front Mater.*, 2021, **8**, 800820, DOI: 10.3389/fmats.2021.800820.
39 A. Khan, M. Ali, A. Ilyas, P. Naik, I. F. J. Vankelecom and M. A. Gilani, *et al.*, ZIF-67 filled PDMS mixed matrix membranes for recovery of ethanol via pervaporation, *Sep. Purif. Technol.*, 2018, **206**, 50–58.
40 M. Afkhami-Ardekani, M. R. Naimi-Jamal, S. Doaee and S. Rostamnia, Solvent-Free Mechanochemical Preparation of Metal-Organic Framework ZIF-67 Impregnated by Pt Nanoparticles for Water Purification, *Catalysts*, 2023, **13**(1), 1–9, DOI: 10.3390/catal13010009.
41 J. R. Xavier, J. R. Beryl, S. P. Vinodhini and G. B. Janaki, Enhanced Protective and Mechanical Properties of Polypyrrole Coatings Modified by Silane/CoO Nanocomposite on AZ91 Mg Alloy in Chloride Media, *J. Bio Tribocorros*, 2021, **7**(2), 46, DOI: 10.1007/s40735-021-00479-7.
42 R. Turczyn, K. Krukiewicz, A. Katunin, J. Sroka and P. Sul, Fabrication and application of electrically conducting composites for electromagnetic interference shielding of remotely piloted aircraft systems, *Compos. Struct.*, 2020, **232**, 111498, DOI: 10.1016/j.compstruct.2019.111498.
43 A. H. Birniwa, A. S. Abubakar, A. K. O. Huq and H. N. M. E. Mahmud, Polypyrrole-polyethyleneimine (PPy-PEI) nanocomposite: an effective adsorbent for nickel ion adsorption from aqueous solution, *J. Macromol. Sci., Part A: Pure Appl.Chem.*, 2021, **58**(3), 206–217.
44 A. Khan, M. Ali, A. Ilyas, P. Naik, I. F. J. Vankelecom and M. A. Gilani, *et al.*, ZIF-67 filled PDMS mixed matrix membranes for recovery of ethanol via pervaporation, *Sep. Purif Technol.*, 2018, **206**, 50–58, DOI: 10.1016/j.seppur.2018.05.055.
45 Y. Li, J. Li, Y. Dai, X. Li, C. Shao and Y. Sun, *et al.*, Co_3O_4@carbon with high Co^{2+}/Co^{3+} ratios derived from ZIF-67 supported on N-doped carbon nanospheres as stable bifunctional oxygen catalysts. Mater Today, *Energy*, 2021, **21**, 100737, DOI: 10.1016/j.mtener.2021.100737.
46 H. Chen, X. Wu, R. Zhao, Z. Zheng, Q. Yuan and Z. Dong, *et al.*, Preparation of reduced graphite oxide loaded with cobalt(II) and nitrogen co-doped carbon polyhedrons from a metal–organic framework (type ZIF-67), and its application to electrochemical determination of metronidazole, *Microchim. Acta*, 2019, **186**(9), 623, DOI: 10.1007/s00604-019-3737-6.
47 W. Shao, Y. R. Chen, F. Xie, H. Zhang, H. T. Wang and N. Chang, Facile construction of a ZIF-67/AgCl/Ag heterojunction: via chemical etching and surface ion exchange strategy for enhanced visible light driven photocatalysis, *RSC Adv.*, 2020, **10**(63), 38174–38183.
48 X. H. Li, P. He, T. Wang, X. W. Zhang, W. L. Chen and Y. G. Li, Keggin-Type Polyoxometalate-Based ZIF-67 for Enhanced Photocatalytic Nitrogen Fixation, *ChemSusChem*, 2020, **13**(10), 2769–2778.
49 S. Rehman, R. Ahmed, K. Ma, S. Xu, T. Tao and M. A. Aslam, *et al.*, Composite of strip-shaped ZIF-67 with polypyrrole: a conductive polymer-MOF electrode system for stable and high specific capacitance, *Eng. Sci.*, 2021, **13**, 71–78.
50 Y. Li, Z. Jin and T. Zhao, Performance of ZIF-67 – Derived fold polyhedrons for enhanced photocatalytic hydrogen evolution, *Chem. Eng. J.*, 2020, **382**, 123051, DOI: 10.1016/j.cej.2019.123051.
51 M. A. Chougule, G. D. Khuspe, S. Sen and V. B. Patil, Polypyrrole–ZnO nanohybrids: effect of CSA doping on structure, morphology and optoelectronic properties, *Appl. Nanosci.*, 2013, **3**(5), 423–429.
52 H. Song, K. Cai, J. Wang and S. Shen, Influence of polymerization method on the thermoelectric properties of multi-walled carbon nanotubes/polypyrrole composites, *Synth. Met.*, 2016, **211**, 58–65.
53 R. Nayak, P. Shetty, M. Selvakumar, A. Rao, K. M. Rao and S. Mangavati, *et al.*, Enhancement of power factor of screen printed polyaniline/graphite based flexible thermoelectric generator by structural modifications, *J. Alloys Compd.*, 2022, **922**, 166298, DOI: 10.1016/j.jallcom.2022.166298.

54 J. Chen and L. Meng, Effects of Different Phonon Scattering Factors on the Heat Transport Properties of Graphene Ribbons, *ACS Omega*, 2022, **7**(23), 20186–20194.
55 Y. Du, J. Xu, B. Paul and P. Eklund, Flexible thermoelectric materials and devices, *Appl. Mater. Today*, 2018, **12**, 366–388.
56 Y. Li, Y. Gao, X. Cao, X. Rong, B. Chen and G. Tian, *et al.*, Encapsulation and thermal properties of composite phase change materials based on cobalt/nitrogen double-doped ZIF-67 derived carbon, *RSC Adv.*, 2023, **13**(38), 26907–26917.
57 J. Gao, C. Liu, L. Miao, X. Wang, C. Li and R. Huang, *et al.*, Power factor enhancement via simultaneous improvement of electrical conductivity and Seebeck coefficient in tellurium nanowires/reduced graphene oxide flexible thermoelectric films, *Synth. Met.*, 2015, **210**, 342–351.
58 S. Shin, R. Kumar, J. W. Roh, D. S. Ko, H. S. Kim and S. Il Kim, *et al.*, High-Performance Screen-Printed Thermoelectric Films on Fabrics, *Sci. Rep.*, 2017, **7**, 7317, DOI: 10.1038/s41598-017-07654-2.
59 D. Ding, F. Sun, F. Xia and Z. Tang, A high-performance and flexible thermoelectric generator based on the solution-processed composites of reduced graphene oxide nanosheets and bismuth telluride nanoplates, *Nanoscale Adv.*, 2020, **2**(8), 3244–3251.
60 R. J. Williams, P. J. Smith and C. Majewski, Is ink heating a relevant concern in the High Speed Sintering process?, *Int. J. Adv. Manuf. Technol.*, 2021, **113**(3–4), 1073–1080.
61 J. Du, B. Zhang, M. Jiang, Q. Zhang, K. Zhang and Y. Liu, *et al.*, Inkjet Printing Flexible Thermoelectric Devices Using Metal Chalcogenide Nanowires, *Adv. Funct. Mater.*, 2023, **33**(26), 2213564, DOI: 10.1002/adfm.202213564.
62 S. Zarabi Golkhatmi, P. D. Lund and M. I. Asghar, A novel $CuFe_2O_4$ ink for the fabrication of low-temperature ceramic fuel cell cathodes through inkjet printing, *Mater. Adv.*, 2023, **5**(1), 143–158.
63 S. Shetty, M. Saquib, M. Selvakumar, H. Firouzi and R. Nayak, Graphene-enhanced manganese dioxide functional ink infused with polyaniline for high-performance screen-printed micro supercapacitor, *Mater. Res. Express*, 2024, **11**(8), 085503, DOI: 10.1088/2053-1591/ad674e.
64 P. Arya, Y. Wu, F. Wang, Z. Wang, G. Cadilha Marques and P. A. Levkin, *et al.*, Wetting Behavior of Inkjet-Printed Electronic Inks on Patterned Substrates, *Langmuir*, 2024, **40**(10), 5162–5173.
65 H. Konno, M. Omata, K. Kikuchi, M. Gotou, K. Yasuda and A. Wakisaka, Size-controlled synthesis of zeolitic imidazolate framework-67 (ZIF-67) using electrospray in liquid phase, *Chem. Lett.*, 2020, **49**(8), 875–878.
66 N. V. Blinova, J. Stejskal, M. Trchová, J. Prokeš and M. Omastová, Polyaniline and polypyrrole: a comparative study of the preparation, *Eur. Polym. J.*, 2007, **43**(6), 2331–2341.
67 X. Zhang and L. D. Zhao, Thermoelectric materials: energy conversion between heat and electricity, *J. Materiomics*, 2015, **1**, 92–105.
68 M. Bharti, A. Singh, S. Samanta, A. K. Debnath, D. K. Aswal and K. P. Muthe, *et al.*, Flexo-green Polypyrrole – Silver nanocomposite films for thermoelectric power generation, *Energy Convers Manage.*, 2017, **144**, 143–152.
69 K. A. Morgan, T. Tang, I. Zeimpekis, A. Ravagli, C. Craig and J. Yao, *et al.*, High-throughput physical vapour deposition flexible thermoelectric generators, *Sci. Rep.*, 2019, **9**, 4393, DOI: 10.1038/s41598-019-41000-y.
70 J. Y. Oh, J. H. Lee, S. W. Han, S. S. Chae, E. J. Bae and Y. H. Kang, *et al.*, Chemically exfoliated transition metal dichalcogenide nanosheet-based wearable thermoelectric generators, *Energy Environ. Sci.*, 2016, **9**(5), 1696–1705.
71 R. Nayak, P. Shetty, M. Selvakumar, B. Shivamurthy, A. Rao and K. V. Sriram, *et al.*, Influence of microstructure and thermoelectric properties on the power density of multi-walled carbon nanotube/metal oxide hybrid flexible thermoelectric generators, *Ceram. Interfaces*, 2023, **49**(23), 39307–39328.
72 P. A. Yoshitha, M. R. Shankar, A. N. Prabhu, R. Nayak, A. Rao and G. Poojitha, Fabrication and characterisation of a flexible thermoelectric generator using PANI/graphite/bismuth telluride composites, *RSC Adv.*, 2024, **14**(54), 40117–40132.
73 V. Pal, P. R. Sreeram, S. S. Legese, P. Srivastava, R. Rohini and K. Chattopadhyay, *et al.*, Understanding the interface-driven thermoelectric behaviour of Bi_2Te_3–Ga_2Te_3 alloys, *J. Phys. Chem. Solids*, 2025, **207**, 112904, DOI: 10.1016/j.jpcs.2025.112904.
74 X. Chen, L. Feng, P. Yu, C. Liu, J. Lan and Y. H. Lin, *et al.*, Flexible Thermoelectric Films Based on Bi_2Te_3 Nanosheets and Carbon Nanotube Network with High n-Type Performance, *ACS Appl. Mater. Interfaces*, 2021, **13**(4), 5451–5459.
75 T. Chiba, H. Yabuki and M. Takashiri, High thermoelectric performance of flexible nanocomposite films based on Bi_2Te_3 nanoplates and carbon nanotubes selected using ultracentrifugation, *Sci. Rep.*, 2023, **13**(1), 3010, DOI: 10.1038/s41598-023-30175-0.
76 D. Ding, F. Sun, F. Xia and Z. Tang, A high-performance and flexible thermoelectric generator based on the solution-processed composites of reduced graphene oxide nanosheets and bismuth telluride nanoplates, *Nanoscale Adv.*, 2020, **2**(8), 3244–3251.
77 Q. Jin, S. Jiang, Y. Zhao, D. Wang, J. Qiu and D. M. Tang, *et al.*, Flexible layer-structured Bi_2Te_3 thermoelectric on a carbon nanotube scaffold, *Nat. Mater.*, 2019, **18**(1), 62–68.